Imbibition and evaporation of droplets of colloidal suspensions on permeable substrates

Truong Pham and Satish Kumar

Imbibition and Evaporation of Droplets of Colloidal Suspensions on Permeable Substrates

Truong Pham and Satish Kumar[1]

Department of Chemical Engineering and Materials Science, University of Minnesota,

Minneapolis, MN 55455

Abstract - When evaporated on a substrate, a droplet containing solutes usually deposits the solutes onto the substrate in a "coffee-ring" pattern. Recent experiments have shown that substrate permeability can suppress the coffee-ring pattern and promote more uniform solute deposition. Motivated by these observations, we have developed a lubrication-theory-based model to describe imbibition and evaporation of droplets of colloidal suspensions on permeable substrates. The model consists of a system of one-dimensional partial differential equations accounting for the changing droplet shape and depth-averaged concentration of colloidal particles. We also incorporate a precursor film, disjoining pressure, and substrate topography to control contact-line motion of the droplet. Solvent evaporation is described using the well-known one-sided model, and imbibition of solvent by the substrate is assumed to only depend on the excess pressure on the liquid side. The governing equations are solved with finite-difference methods. Our results reveal that solvent evaporation and solvent imbibition have the same qualitative effect on the final particle deposition pattern. For the case where the substrate is smooth, we find that increasing imbibition or evaporation leads to a transition from a cone-shaped deposition pattern to a ring-shaped deposition pattern. For the case where the substrate is rough, the droplet contact line is pinned at a defect on the substrate, and the pinning-depinning transition leads to the "bullseye" deposition pattern often observed in experiments. Finally, we also find that particle adsorption onto the substrate can promote more uniform particle deposition patterns for both smooth and rough substrates, and solvent imbibition can indirectly suppress the coffee-ring pattern by inducing more particle adsorption.

[1]E-mail address for correspondence: kumar030@umn.edu

1 Introduction

1.1 Motivation

It is an everyday sight to see an evaporated coffee droplet deposit a ring-like pattern on a solid substrate. Since first investigated by Deegan and coworkers [1], the "coffee-ring" effect has attracted considerable scientific interest due to its robustness and potential technological applications in ink-jet printing [2], spray coating [3,4], microfabrication [5–7], and bio-assays [8–10]. The ability to control the final deposition pattern of solutes in drying droplets is of significant technological importance.

In many popular applications such as printing on textiles, drug coating, and fabrication of paper-based sensors, the substrates used are made of permeable materials (e.g., sintered powder, gel, woven fibers) [11–14]. When a droplet carrying solutes is deposited on such a substrate, imbibition of solvent inside the droplet by the substrate can be just as important as evaporation of solvent in controlling solute deposition. Whereas the bulk of coffee-ring-related literature has focused on systems where the underlying solid surfaces are impermeable, relatively few experimental studies have looked into the effect of substrate permeability on solute deposition patterns [11,12,15,16], and to the best of our knowledge, systematic theoretical investigations of this problem are non-existent.

1.2 Review of previous work

Studies on imbibition of droplets and those on evaporation of droplets rarely overlap, but it appears from numerous experimental reports that both imbibition and evaporation of pure-solvent droplets produce qualitatively similar contact-line dynamics [17–26]. When a pure-solvent droplet is evaporated or imbibed on a horizontal substrate, the contact line of the droplet can, in general, go through three stages. The first stage is a pinned or locked stage, where the contact-line position remains fixed whereas the contact angle decreases due

to loss of solvent. When the contact-angle becomes small enough, the contact line begins to recede toward the center of the droplet. During this second stage, the contact angle stays relatively constant. Finally, in the third stage, both droplet radius and contact angle precipitously drop to zero.

The majority of mathematical models for evaporation and imbibition of droplets have treated different stages of contact-line dynamics separately [18, 27–41]. To describe each stage, constraining assumptions are often imposed such as requiring the droplet to have a spherical-cap shape in the pinned stage or constant contact angle in the receding stage [18, 19, 42–44]. Even though treating these stages separately enables understanding of transport processes in systems where one stage dominates the others, in doing so one may also miss important dynamics happening when one stage transitions to another, or when all stages are equally important.

Two recent studies have demonstrated that incorporating substrate roughness into a lubrication-theory-based droplet model allows one to capture all the stages of contact-line dynamics for a pure-solvent droplet being imbibed or evaporated [45, 46]. By incorporating a precursor film and disjoining pressure to control contact-line dynamics, the resulting models are able to capture all three stages with no assumptions (apart from lubrication theory) made regarding droplet shape or contact angle. There are two advantages to this approach. First, it allows the models to readily be extended to much more general situations (e.g., droplets on inclined surfaces) where the spherical-cap assumption is no longer valid [33, 47, 48]. Second, it enables a natural description of the transition from the pinned stage to the receding stage instead of treating the two stages separately.

Moreover, the ability to capture all stages of contact-line motion reveals the significant influence of contact-line motion on the final particle deposition pattern [46]. When substrate roughness is negligible, the pinned stage is absent and colloidal particles will be transported to the droplet center, resulting a cone-like deposit. When the pinned stage is present,

colloidal particles are transported to the droplet edge, resulting in a ring-like deposit. These results agree well with recent experimental observations made by Morales *et al.* [49] and Das *et al.* [50], where the authors demonstrated that the final solute deposition pattern from a drying droplet strongly depends on the dominant mode of contact-line motion.

Although pure-solvent droplets undergoing imbibition and evaporation have similar contact-line dynamics, imbibed droplets of colloidal suspensions have been observed to leave behind particle deposition patterns that are drastically different from the coffee-ring pattern [11,12,15,16]. For example, Pack *et al.* observed droplets of polystyrene particles undergoing simultaneous evaporation and imbibition on porous aluminum oxide substrates [15]. They reported that when solvent imbibition is much faster than solvent evaporation, the coffee-ring pattern is suppressed, and droplets leave behind more uniform deposit patterns. Even though these experimental studies have shown a correlation between solvent imbibition and coffee-ring suppression, the physical mechanisms behind this observation are still unclear. To understand these mechanisms, it will be helpful to develop a mathematical model that can help us delineate different processes occurring as droplets of colloidal suspensions are evaporated and imbibed.

1.3   Overview of the paper

In the present paper, we seek to extend the models in Refs. [45, 46] to describe transport of colloidal particles inside droplets undergoing both evaporation and imbibition. Our objective is to determine whether solvent evaporation and solvent imbibition have different effects on the final particle deposition pattern. The rest of the paper is organized as follows. The mathematical model is constructed in Section 2, and reference cases of evaporation and imbibition of pure-solvent droplets are established in Section 3. We then perform a parametric study on the effect of varying evaporation and imbibition rates on perfectly smooth substrates in Section 4, and discuss the influence of surface roughness in Section

4

5. The important role of particle adsorption onto the substrate is discussed in Section 6. Finally, concluding remarks are offered in Section 7.

2 Mathematical model

In this section, we derive the evolution equations governing droplet shape and particle concentration. We discuss hydrodynamics (Section 2.1), imbibition (Section 2.2), evaporation (Sections 2.3 and 2.4), particle transport (Section 2.5), and our solution method (Section 2.6).
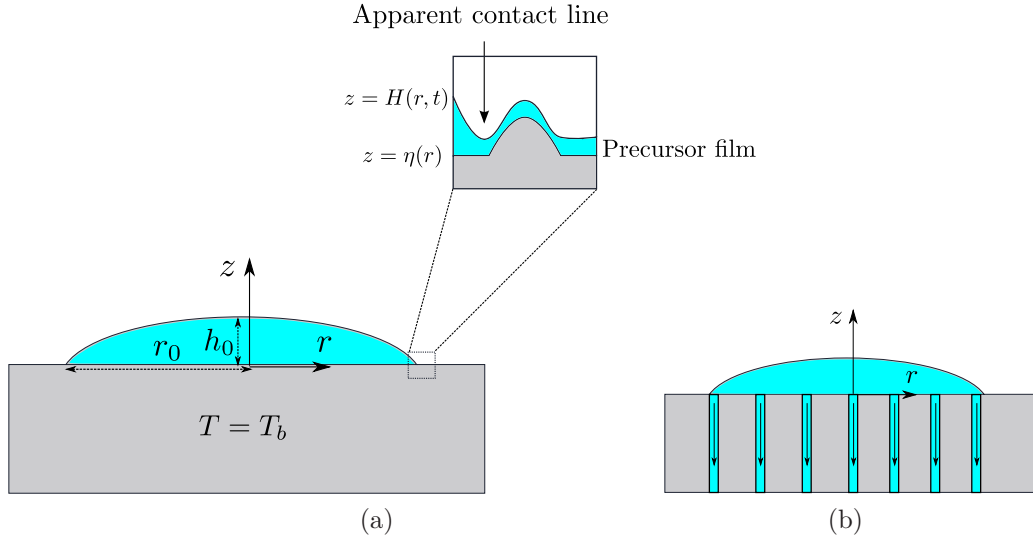

Figure 1: (a) A droplet on top of a permeable substrate. A precursor film is present near the droplet edge, and the substrate may have topographical features. (b) Cross section of the system: pores inside the substrate are saturated with liquid.

2.1 Hydrodynamics

We consider an axisymmetric droplet consisting of a Newtonian liquid and colloidal particles on a horizontal substrate (Fig. 1a). The radial and vertical coordinates are denoted by r and z, respectively. A precursor film is present near the droplet edge, and its constant thickness

far away from the droplet is denoted by b. The liquid velocity is $\mathbf{v} = u\hat{\mathbf{e}}_r + w\hat{\mathbf{e}}_z$, where $\hat{\mathbf{e}}_r$ and $\hat{\mathbf{e}}_z$ are unit vectors in the r- and z-directions. The underlying substrate topography is specified by $\eta(r)$, and the liquid-vapor interface is located at $H(r,t) = \eta(r) + h(r,t)$, where $h(r,t)$ is the thickness of the droplet.

The characteristic radial and vertical length scales of the droplet are $r^* = r_0$ and $z^* = h_0$, where r_0 is its initial radius and h_0 is the maximum droplet thickness. The precursor film thickness b is 10^2 to 10^4 times smaller than h_0 [51]. Substrate topography varies on length scales comparable to b and is expressed as $\eta(r)$.

The droplet is assumed to be thin so that its characteristic lengths r_0 and h_0 satisfy $\epsilon = h_0/r_0 \ll 1$, allowing us to apply lubrication theory. The characteristic time is taken to be the time for capillary-driven spreading, $t^* = 3\mu_0 r^*/\sigma_0\epsilon^3 \equiv t_c$, where μ_0 and σ_0 are the viscosity and surface tension of the pure solvent. The horizontal velocity scale is $u^* = r^*/t^*$, and the pressure scale is $p^* = h^*\sigma_0/r^{*2}$. We apply these scales to obtain the following dimensionless variables (henceforth denoted with primes):

$$r = r^*r', \; z = h^*z', \; u = u^*u', \; w = \epsilon u^*w'$$
$$t = t^*t', \; p = p^*p'. \tag{1}$$

The time-evolution of the droplet shape can be described using the leading-order kinematic boundary condition, which accounts for conservation of mass at the interface $H(r,t) = \eta(r) + h(r,t)$,

$$h'_{t'} = w' - u'(h' + \eta')_{r'} - Ej'_e, \tag{2}$$

where the subscripts r' and t' denote partial derivatives. Here, j'_e is the evaporation flux, and $E = t_c/t_e$ is the evaporation number, the ratio between the characteristic capillary and evaporation times. Specific expressions for the evaporation time t_e and the evaporation flux j_e will be given in Section 2.4 where we discuss energy transport.

In Eq. (2), the velocity components w' and u' are evaluated at the interface, which requires us to express w' and u' as functions of z'. To proceed, we solve the leading-order mass and momentum conservation equations:

$$-3p'_{r'} + (Mu')_{z'z'} = 0, \tag{3}$$

$$p'_{z'} = 0, \tag{4}$$

$$w'_{z'} + \frac{1}{r'}(r'u')_{r'} = 0, \tag{5}$$

where the subscripts r' and z' denote spatial derivatives, and M is the viscosity of the droplet. Assuming the particles are hard spheres, we use the well-known Krieger-Dougherty relationship [52] to relate the viscosity μ to the particle volume fraction c,

$$M = \frac{\mu}{\mu_0} = \left(1 - \frac{c}{0.64}\right)^{-2}. \tag{6}$$

At the random-packing limit of $c = 0.64$, the viscosity of the colloidal suspension diverges, and the droplet is assumed to be solidified. In deriving Eqs. (3) and (4), we also assume that gravitational effects are small compared to surface-tension effects.

To solve for the horizontal velocity component u', we impose the no-slip boundary condition at the substrate-liquid interface $z' = \eta'$ (Eq. (7)), and tangential and normal stress balances at the liquid-vapor interface $z' = h' + \eta' = H'$ (Eqs. (8)-(9)),

$$u'|_{z'=\eta'} = 0, \tag{7}$$

$$u'_{z'}|_{z'=H'} = 0, \tag{8}$$

$$p'|_{z'=H'} - p'_v = -H'_{r'r'} - \frac{H'_{r'}}{r'} - \Pi', \tag{9}$$

where p'_v is the pressure in the vapor phase. The first two terms on the right-hand side of Eq.

7

(9) account for capillary pressure in the droplet, which is proportional to the mean curvature of the droplet surface. The final term Π' of Eq. (9) represents the disjoining pressure, which controls the contact-line motion of the droplet.

To overcome the conflict between the no-slip boundary condition and a moving contact line, two general approaches to model moving contact lines have been proposed. The first approach uses a slip law that relates a finite contact-line speed to some microscopic slip length [53–57]. This approach requires both the velocity field and the contact-line position to be solved.

The second approach assumes that there is a thin precursor film between the bulk liquid and the substrate. In this precursor film, disjoining pressure—which arises from short-range interactions between liquid, solid, and vapor molecules—becomes significant and can be modified to control the apparent contact angle while allowing a moving apparent contact line. Schwartz *et al.* appear to be the first to have taken this approach [58,59]. Disjoining pressure and precursor films have been used to study droplet dynamics in various contexts, including evaporation and imbibition of pure sessile liquid droplets [27–29, 45], droplet spreading on substrates with topography [53, 60], and drying of droplets of colloidal suspensions [30, 32, 33, 61]. The principal advantage of this approach over the first one is that the resulting equations are much easier to solve [53]. This is because the contact-line position is not an explicit unknown; it can be extracted from the droplet height profile (see Appendix).

To account for partial wetting, we use a two-term disjoining-pressure expression,

$$\Pi' = A_1 \left(\left(\frac{A_2}{h'} \right)^n - \left(\frac{A_2}{h'} \right)^m \right), \tag{10}$$

where $A_1 > 0$ is the dimensionless Hamaker constant, which describes the magnitude of the energy of intermolecular interactions, and A_2 is a parameter of the same order of magnitude as the precursor-film thickness. In the absence of evaporation and imbibition, A_2 can be set equal to the precursor-film thickness far away from the droplet. A discussion of how a

8

non-zero precursor-film thickness is maintained in the presence of evaporation and imbibition is provided in Section 2.6. The first and second terms of Eq. (10) describe repulsion and attraction between liquid-vapor and liquid-solid interfaces, respectively [62]. We choose $n = 3$ and $m = 2$ because previous works have shown that these values provide an adequate description of partial wetting at a reasonable computational cost [39, 40, 45].

To solve for the vertical velocity component w', we would need to specify a boundary condition for w' at the liquid-solid interface, which requires some assumptions regarding liquid imbibition.

2.2 Imbibition

For liquid imbibition, we use a model proposed by Espín and Kumar [45],

$$w'|_{z'=0} = -Ij'_i = I(\Pi' + h'_{r'r'} + \frac{h'_{r'}}{r'}), \tag{11}$$

where the imbibition number is defined as $I = 3\kappa/\epsilon^2 h_0 d$. Here, κ is the permeability constant, which has units of length squared, and d is the thickness of the permeable substrate. The imbibition number can be interpreted as the ratio between the characteristic capillary time scale t_c (Section 2.1) and the imbibition time scale, $t_I = \kappa\sigma_0/\mu dr_0^2$.

This model was originally used by Davis and Hocking to describe droplet imbibition on a permeable substrate with unconnected, saturated cylindrical pores [63]. The original model assumes that excess liquid pressure above the substrate drives Poiseuille flows in the pores while neglecting any entry or exit effects. Thus, the permeability constant, $\kappa = \pi\Gamma_{pore}r_{pore}^4/8$, depends on the area density of pores Γ_{pore} and the pore radius r_{pore}. Because the substrate is assumed to be saturated, κ does not depend on pore wettability (contact angle).

Since the original model would make the precursor film disappear under the action of excess pressure *above the substrate*, it was modified by Espín and Kumar to describe im-

9

bibition due to excess pressure *above the precursor film.* As a result, the precursor-film thickness away from the contact line can remain constant as the droplet is absorbed into the substrate [45]. The modified imbibition model exhibits regimes of contact-line motion that agree qualitatively with experimental observations [25, 45]. A more detailed discussion of the assumptions of this imbibition model can be found in Ref. [45].

2.3   Evaporation

We describe evaporation using a model based on the kinetic theory of gases. Evaporation is assumed to be limited by how fast the solvent molecules escape the liquid phase and enter the vapor phase [27, 28, 31, 33, 64–69]. In this approach, temperature and pressure differences across the interface drive evaporation. Because this model only requires solving transport equations on the liquid side to obtain the evaporation rate, it is often referred to as the one-sided model.

Another evaporation model that assumes evaporation to be limited by diffusion of solvent vapor in air has been used by many authors [1, 44, 68, 70, 71]. This approach is more computationally expensive than the one-sided model because a diffusion equation for solvent vapor concentration in air has to be solved simultaneously with other transport equations in the droplet. To reduce the computational cost associated with calculating the evaporation flux, the droplet is often assumed to be a spherical cap. More detailed discussions on the different approaches to modeling evaporation can be found in Refs. [31, 72, 73].

The expression for the evaporation flux of the one-sided model was first introduced by Schrage to describe evaporation of a liquid into a uniformly saturated vapor phase [74]. Since then its linearized form has been used in studies of drying thin films [64–66, 69, 72, 75, 76] and droplets [27, 28, 30–34],

$$\frac{\sqrt{2\pi \hat{R} T_{sat}}}{\rho_v} j_e = \frac{1}{\rho_l}(p - p_v) + \frac{\hat{L}a}{T_{sat}}(T_i - T_{sat}), \tag{12}$$

where $\hat{R}$ is the ideal gas constant per unit mass, $\hat{La}$ is the latent heat of vaporization per unit mass, T_i is the temperature at the liquid-vapor interface, and ρ_l and ρ_v are the densities of the solvent in liquid and vapor forms. The partial pressure of the solvent in the gas phase is p_v, and the saturation temperature T_{sat} can be calculated from the Clausius-Clapeyron equation using p_v as the saturation pressure [29]. From Eq. (12), it can be seen that the evaporation flux j_e is proportional to deviations from p_v and T_{sat}.

Because Eq. (12) was originally used to describe evaporation of a one-component system, it may not quantitatively reflect evaporation for a droplet laden with particles. However, work by Cazabat and Guena hinted that the one-sided model is expected to be more accurate at describing evaporating droplets contaminated with other species, since contamination makes the rate-limiting step more likely to be in the liquid phase, which is the primary assumption of the one-sided model [68]. Owning to its simplicity, Eq. (12) has been used to study the qualitative behavior of drying multicomponent thin films and droplets in previous studies [30, 32–34, 65].

2.4 Energy transport

The substrate is held at a constant temperature T_b, and temperature is scaled as $T' = (T - T_{sat})/(\epsilon^2 T_{sat})$. The leading-order energy transport equation is

$$T'_{z'z'} = 0. \tag{13}$$

When the density, viscosity, and thermal conductivity of the liquid are much higher than those of the vapor, it can be shown that the dominant mechanism for heat dissipation is through vaporizing the liquid [64]. After balancing the conductive heat within the droplet with the heat transported out by evaporation, we obtain a scaling factor for j, $j^* = \epsilon^2 k T_{sat}/h_0 \hat{La}$, where k is the thermal conductivity of the droplet. From this scaling, we

can obtain an expression for the evaporation time, $t_e = h_0\rho_l/j^*$. As have previous works, we assume that the thermal conductivity of the droplet does not depend on the concentration of colloidal particles [30, 32–34, 65]. The dimensionless temperature boundary conditions are

$$T'|_{z'=\eta'} = 1, \tag{14}$$

$$-T'_{z'}|_{z'=H'} = j'_e.$$

Solving Eq. (13) while imposing the boundary conditions in Eq. (14) gives

$$j'_e = \frac{1 + \delta(p' - p'_v)}{K + h'}, \tag{15}$$

where

$$K = \frac{\sqrt{2\pi\hat{R}T_{sat}}kT_{sat}}{\rho_v\hat{La}^2h_0\epsilon^2}, \ \delta = \frac{\sigma_0}{\rho_l\hat{La}r_0\epsilon}. \tag{16}$$

As shown in previous studies [33, 46, 69], this energy transport model results in an interfacial temperature inversely proportional to the local droplet thickness. Therefore, there are temperature gradients at the liquid-vapor interface that drive thermal Marangoni flows from thin droplet regions (i.e., near contact line) to thick droplet regions (i.e., near droplet center), accelerating contact-line retraction. However, thermal Marangoni effects are neglected in this work when solvent evaporation is present because calculations including them show that they do not change the qualitative trends we observe.

2.5 Colloidal particle transport and evolution equations

Assuming no particles are adsorbed at the droplet surface or substrate, we impose no-flux boundary conditions for particle concentration at the liquid-solid and liquid-vapor interfaces,

$$-D\nabla c' + (\mathbf{v}' - \mathbf{v}'_I)c' = 0, \tag{17}$$

12

where $\mathbf{v}'_I$ is the velocity of the interface. In Section 6, we will modify this no-flux boundary condition to allow particle adsorption onto the substrate.

Following a procedure similar to those in Refs. [46, 77], we obtain the leading-order transport equation for the z-averaged concentration of particles $\bar{c}$:

$$\bar{c} = \frac{1}{h'} \int\limits_{\eta'}^{\eta'+h'} c \, dz',$$

(18)

$$\bar{c}_t + \bar{u}\bar{c}_r = \frac{1}{hrPe}(Dhr\bar{c}_r)_r + \frac{\bar{c}}{h}(Ej_e + Ij_i).$$

(19)

In writing Eq. (19), we have dropped the prime superscripts to simplify the notation, a convention we will follow for the rest of the paper. Here, the diffusion coefficient D as a function of particle concentration c is given by the expression [52, 78, 79]

$$D = D_0(1-c)^{6.55}\frac{d}{dc}\left(\frac{1.85c}{0.64-c}\right),$$

(20)

where D_0 is the Stokes-Einstein diffusivity [52],

$$D_0 = \frac{k_B T_{sat}}{6\pi\mu_0 a},$$

(21)

with k_B being Boltzmann's constant and a the particle radius. At low particle concentrations, D is a decreasing function of particle concentration due to hydrodynamic interactions between the particles. At high particle concentrations, hard-sphere repulsion becomes dominant and D diverges at the random-packing limit $c = 0.64$ [52, 80].

Eq. (19) is derived based on the assumption that strong diffusion quickly levels out particle concentration gradients in the z-direction. This condition can be expressed mathematically as $\epsilon^2 Pe \ll 1$, where the Péclet number $Pe = u^* r_0/D_0$ gives the ratio between the diffusive time scale and the convective (capillary) time scale for transport of colloidal parti-

cles in the radial direction. For the rest of the paper, we will denote the z-average particle concentration $\bar{c}$ as c for simplicity and also rescale c with the maximum volume fraction of 0.64.

In Eq. (19), $\bar{u}$ is the z-averaged radial velocity component, where u as a function of time and spatial variables can be derived from Eq. (3) and boundary conditions (7) and (9),

$$u = -\frac{(h_{rr} + h_r/r + \Pi)_r}{M}\left(\frac{3}{2}z^2 - 3(h+\eta)z - \frac{3}{2}\eta^2 + 3(h+\eta)\eta\right). \tag{22}$$

We can also integrate the continuity equation (Eq. (5)) in z and impose the imbibition boundary condition in Eq. (11) to get the vertical velocity component w. Finally, we can rewrite the right-hand side of the kinematic boundary condition (Eq. (2)) for the droplet thickness h as a function of h and its spatial derivatives,

$$h_t = \frac{1}{r}\left(\frac{rh^3}{M}\left(-A_1\left(\left(\frac{A_2}{h}\right)^3 - \left(\frac{A_2}{h}\right)^2\right) - (h+\eta)_{rr} - \frac{1}{r}(h+\eta)_r\right)_r\right)_r - Ej_e - Ij_i. \tag{23}$$

Equations (19) and (23) are the evolution equations we will solve numerically to obtain the droplet shape and particle concentration at different times when evaporation and imbibition take place.

Without evaporation and imbibition, wetting forces will make a droplet spread on a solid substrate until an equilibrium contact angle is achieved. A small equilibrium contact angle θ_e can be related to constants A_1 and A_2 in Eq. (10) through the following expression [45, 58]:

$$\theta_e \approx \tan(\theta_e) \approx \epsilon\tan(\theta'_e) \approx \epsilon\tan(\sqrt{A_1 A_2}) \approx \epsilon\sqrt{A_1 A_2}. \tag{24}$$

Here, θ_e and θ'_e are the actual (lab-frame) and scaled (based on lubrication theory) contact angles, respectively. In presenting our results, we will report the actual contact angles rather than the scaled ones using a representative value of $\epsilon = 0.1$. More details on how the contact

line and contact angles observed from different length scales are defined can be found the Appendix.

2.6 Parameter values and numerical methods

Typical values of important physical parameters are given in Table 1. Assuming $\epsilon = 0.1$ and $r_0 = 10^{-3}$ m, we can estimate the capillary time (Section 2.1) as $t_c \sim 10^{-2}$ s and the evaporation time (Section 2.4) as $t_e \sim 10 - 10^2$ s, which corresponds to an evaporation number (Section 2.1) $E \sim 10^{-4} - 10^{-3}$.

If the pores are randomly distributed on the substrate, the maximum pore area fraction (ratio of total pore area to substrate area) is 0.82 [81]. The pore area density Γ_{pore} is the number of pores per substrate area, with the number of pores being the ratio of the total pore area to the area of a single pore. Thus, $\Gamma_{pore} \sim 0.82/r_{pore}^2$. Assuming a pore radius r_{pore} in the range from 10^{-9} m to 10^{-6} m, the substrate permeability κ (Section 2.2) will vary from 10^{-18} m² to 10^{-12} m². These values are consistent with those estimated in other studies [25, 45]. The imbibition number I (Section 2.2) then ranges from 10^{-9} to 10^{-3}. We assume that imbibition is takes place over a time scale comparable to evaporation, and thus consider $I \sim 10^{-4} - 10^{-3}$.

Table 1: Order-of-magnitude estimates of physical parameters. Data are from Refs. [17, 22, 51, 64, 82].

Parameter	Definition	Order-of-magnitude estimate
ρ_l (kg m^{-3})	mass density of liquid phase	10^3
ρ_v (kg m^{-3})	mass density of vapor phase	1
h_0 (m)	maximum droplet height after spreading	$10^{-5} - 10^{-3}$
r_0 (m)	initial droplet radius	$10^{-3} - 10^{-2}$
μ_0 (Pa s)	characteristic dynamic viscosity	10^{-3}
σ_0 (N m^{-1})	characteristic surface tension	$10^{-3} - 10^{-2}$
k (W K^{-1} m^{-1})	thermal conductivity of liquid phase	$10^{-1} - 1$
T_{sat} (K)	saturation temperature	$298 - 323$
La (J kg^{-1})	latent heat of evaporation	10^6
A_1 (Pa)	Hamaker constant	$10 - 10^4$
A_2 (m)	precursor-film thickness	$10^{-8} - 10^{-6}$
a (m)	particle radius	$10^{-8} - 10^{-7}$
r_{pore} (m)	pore radius	$10^{-9} - 10^{-6}$
κ (m^2)	substrate permeability	$10^{-18} - 10^{-12}$
d (m)	substrate thickness	10^{-3}

From the values in Table 1, we can also estimate $K \sim 10^{-3}$-10^{-1}. As have previous studies [27, 32], we choose δ such that a physically realistic yet computationally inexpensive precursor-film thickness can be obtained, $\delta = 10^{-3}$.

For a particle with radius $a = 10^{-8}$ m, the diffusivity D_0 is around 10^{-10} m^2/s. The Péclet number is then $\sim 10^4$-10^6, which indicates that convection dominates diffusion for transport of particles in the radial direction.

Equations (19) and (23) are numerically solved on the domain $0 \leq r \leq 5$ subject to the

boundary conditions

$$h_r(0, t) = h_r(5, t) = h_{rrr}(0, t) = c_r(0, t) = c_r(5, t) = 0, \tag{25}$$

$$h(t, 5) = b, \tag{26}$$

where b, the steady-state thickness of the precursor film, is obtained by numerically solving $Ej_e + Ij_i = 0$, where j_e and j_i are given by Eqs. (15) and (11), respectively. This is an algebraic equation representing a balance between evaporation and imbibition in the precursor-film region. In this region, a solvent flux comes out of the substrate to replenish the solvent loss due to evaporation. For this study, we use a precursor-film thickness $b \sim 10^{-3}h_0$, a value within the range used by previous works [27, 45, 51, 58].

The initial condition for the droplet shape is given by a fourth-order polynomial that satisfies the boundary conditions in Eqs. (25) and (26) at $r = 1$. When colloidal particles are present, the initial condition for particle concentration is given by

$$c = \begin{cases} c_0 & r \leq 1 \\ 0 & r > 1, \end{cases} \tag{27}$$

which describes an experimental situation where a droplet laden with colloidal particles is deposited on a pure-solvent precursor film [30].

On the computational domain $0 \leq r \leq 5$, the spatial derivatives in Eqs. (19) and (23) are approximated with second-order centered finite differences. We typically use between 600 and 1200 nodes per unit length. The resulting discretized system of ordinary differential equations is solved with the implicit time-stepping solver DDASPK [83].

The equilibrium contact angle θ_e for each droplet is obtained by first running simulations on smooth substrates without evaporation and imbibition. For each set of values of A_1 and A_2, the equilibrium contact angle is recorded after the initial spreading stage. These

17

values are then rescaled with $\epsilon = 0.1$ to obtain the lab-frame contact angle (Section 2.5). This procedure allows us to obtain equilibrium contact angles within 1 to 3 degrees of those predicted from Eq. (24).

Each simulation with evaporation and imbibition is stopped when the total volume of the droplet is less than 10^{-3}, or when the particle volume fraction is within 98.4% of the random-packing limit. We have also verified the $t^{1/10}$ scaling law for contact-line speed of perfectly wetting droplets with our code [62, 84]. For brevity, the scaling-law comparison is not shown here.

3   Evaporation and imbibition of pure-solvent droplets

3.1   Evaporation and imbibition fluxes

Before looking at the behavior of droplets laden with particles, it is helpful to review how the shape of a pure-solvent droplet on a substrate evolves as the solvent is evaporated or imbibed by the substrate. To delineate the dynamics due to solvent evaporation and solvent imbibition, we first analyze imbibition and evaporation separately.

Figures 2a and 2b show typical evaporation and imbibition flux profiles, respectively, as functions of r for droplets on perfectly smooth substrates. The evaporation number and imbibition number are set to the same value for these figures: $E = I = 10^{-4}$. We numerically solve for the droplet profiles $H(r)$ at $t = 100$, and the imbibition and evaporation fluxes are calculated using Eqs. (11) and (15).

It can be seen from Figs. 2a and 2b that for similar droplet shapes, the evaporation and imbibition fluxes are of the same order of magnitude. Whereas the evaporation flux increases sharply near the contact line of the droplet, the imbibition flux remains constant within the droplet. This difference can be understood upon inspection of Eqs. (11) and (15). Equation
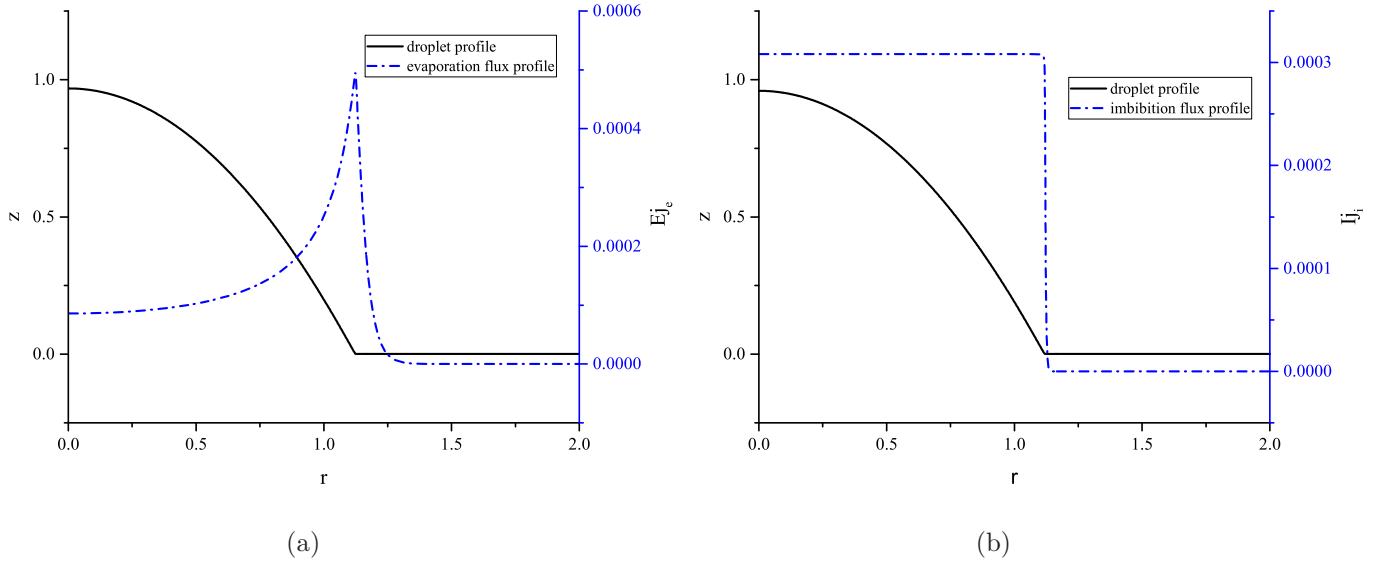
18

Figure 2: (a) Height profile and evaporation flux profile of a pure-solvent droplet on an impermeable substrate. The profiles are recorded at $t = 100$. The evaporation flux is highest near the contact line. Values of parameters are: $\theta_e = 9.42^o$ ($A_1 = 3 \times 10^3$ and $A_2 = 10^{-3}$), $E = 10^{-4}$, $I = 0$, $b = 8.18 \times 10^{-4}$, $K = 2 \times 10^{-1}$, $\delta = 10^{-3}$. (b) Height profile and imbibition flux profile of a non-volatile pure-solvent droplet. The profiles are recorded at $t = 100$. The imbibition flux is relatively uniform inside the droplet. All parameters are the same as in (a) except for: $E = 0$, $I = 10^{-4}$, $b = 1.0 \times 10^{-3}$.

(15) shows that the evaporation flux is inversely proportional to the local droplet thickness h, so the flux should be expected to peak at the contact line where the droplet is thinnest. Notably, even though we use a one-sided evaporation model, our evaporation flux profile is qualitatively similar to that obtained from the diffusion-limited model [31, 42, 85].

In contrast, the expression for the imbibition flux, Eq. (11), shows that imbibition only depends on a the local pressure, which, in the droplet bulk, mostly comes from capillary pressure. Since capillary pressure depends on the curvature of the liquid-vapor interface, and capillary flows quickly level any curvature gradients caused by a much slower imbibition process, the curvature of the droplet remains relatively constant. Thus, the imbibition flux is constant inside the droplet. Next, we examine whether the qualitative difference between the evaporation and imbibition flux profiles leads to any difference in contact-line dynamics of a pure-solvent droplet.

3.2   Contact-line motion

The time-evolution of the radius of a droplet undergoing imbibition and evaporation on a smooth substrate is shown in Fig. 3a. Figure 3a shows that if the substrate is perfectly smooth, both imbibition and evaporation make the droplet contact line recede continuously. We have demonstrated in previous work that this scenario corresponds to the constant-contact-angle stage of contact-line motion when a droplet is either evaporated or imbibed [45, 46]. The faster receding speed for droplet imbibition can be understood by revisiting Fig. 2: the evaporation flux is lower than the imbibition flux, except very close to the contact line. This results in a faster contact-line speed when the droplet is imbibed.

The time-evolution of the droplet radius on a rough substrate is shown in Fig. 3b. Previous work on droplet imbibition and evaporation has demonstrated that although in reality there can be multiple microscopic defects of different sizes and shapes randomly distributed on an actual substrate, the influence of the overall substrate roughness on contact-
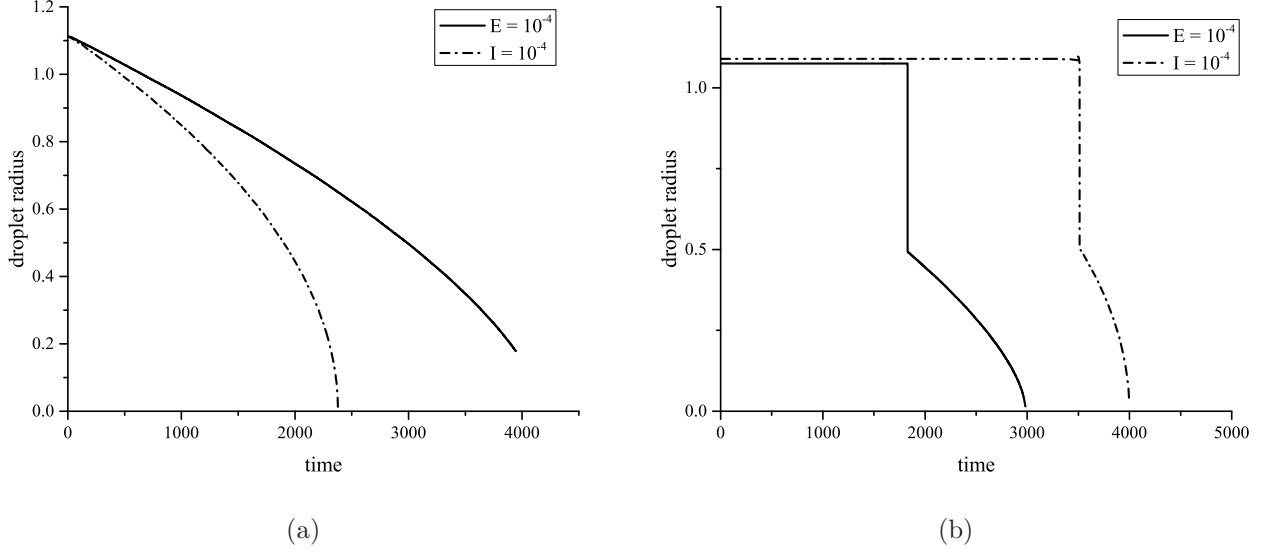
Figure 3: (a) Time-evolution of droplet radius of a pure-solvent droplet on a smooth substrate. Values of parameters are: $\theta_e = 9.42^o$ ($A_1 = 3 \times 10^3$ and $A_2 = 10^{-3}$). For $E = 10^{-4}$ (evaporation only): $b = 8.18 \times 10^{-4}$, $K = 2 \times 10^{-1}$, $\delta = 10^{-3}$. For $I = 10^{-4}$ (imbibition only): $b = 10^{-3}$. (b) Time-evolution of droplet radius of a pure-solvent droplet on a rough substrate. Parameters are the same as in (a), except now the substrate has a Gaussian defect centered at $r = 1.1$.

line motion can be effectively described by using a single defect near the initial contact line of the droplet [45, 46]. Thus, our convenient (albeit arbitrary) choice of the substrate-topography function $\eta(r)$ is a Gaussian bump, $\eta(r) = \eta_0 \exp(-(r-r_d)^2/2s_d^2)$, which describes a single defect centered at r_d with height η_0 and width s_d. To place the defect near the initial location of the contact line ($r = 1$), we set $r_d = 1.1$. We also pick a defect height of $\eta_0 = 5 \times 10^{-2}$ and defect width of $s_d = 10^{-2}$.

When the substrate is rough, the contact-line behavior changes significantly, as can be seen when we compare Figs. 3a and 3b. When a defect is present on the substrate, the contact line is pinned to the defect for some time before "slipping" and retracting toward the droplet center. The pinning of the contact line at the defect has been shown to be a result of a balance between radially outward capillary-pressure gradients and radially inward disjoining-pressure gradients [45, 46]. As the volume of the droplet decreases due to either solvent evaporation or imbibition, this balance is broken at some point, and disjoining-

21

pressure gradients drive the contact line inward. From Fig. 3b, it appears that evaporation leads to an earlier depinning time. This is due to the fact that the evaporation flux at the defect is much higher than the imbibition flux there, which accelerates depinning for evaporation.

Although we focus here on a single defect, we have performed some limited simulations in which multiple defects are present. Here, the droplet contact line may get pinned again at an inner defect after depinning from the outermost defect. This results in a periodic stick-slip motion similar to that reported in previous experiments [17, 21, 21] and simulations [37].

The results in this section have demonstrated that even though there is a qualitative difference between the imbibition flux profile and the evaporation flux profile, this difference does not result in any significant difference in contact-line motion. When the substrate is smooth, the droplet contact line continuously recedes. When the substrate is rough, the droplet contact line is initially pinned and then quickly retracts. This similarity in contact-line behavior for imbibed and evaporated droplets should be expected because imbibition and evaporation are both much slower than capillary flows (i.e., $E = I = 10^{-4}$), so the qualitative difference in flux profiles should not dominate contact-line dynamics.

4 Particle-laden droplets on smooth substrates

The results of Section 3 have shown that even though the imbibition and evaporation flux profiles are qualitatively different, contact-line dynamics remain qualitatively the same for both imbibed and evaporated droplets on smooth and rough substrates. In this section, we will turn our attention to transport of colloidal particles inside a droplet imbibed and evaporated on a perfectly smooth substrate. Because transport of colloidal particles inside evaporating droplets has been discussed in previous works [30, 35, 46], we will only discuss particle transport for droplet imbibition in Section 4.1.
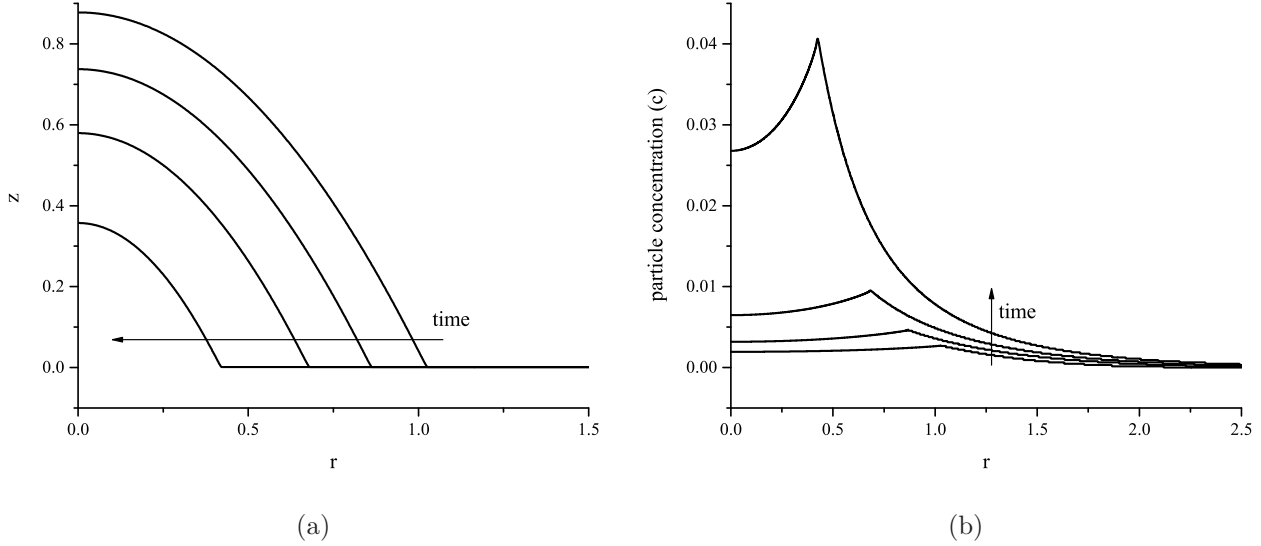
22

4.1 Transport of colloidal particles

Figure 4: Droplet containing colloidal particles imbibed on a smooth substrate. (a) Time-evolution of droplet shape. (b) Time-evolution of particle concentration. Values of parameters are: $\theta_e = 9.42^o$ ($A_1 = 3 \times 10^3$ and $A_2 = 10^{-3}$), $I = 10^{-4}$, $b = 10^{-3}$, $Pe = 10^{-4}$, $c_0 = 10^{-3}$. The profiles are recorded at $t_1 = 469$, $t_2 = 939$, $t_3 = 1409$, and $t_4 = 2338$.

Figure 4 shows the time-evolution of droplet shape and particle concentration profiles as a droplet is imbibed on a smooth substrate. Here, the particle concentration has been rescaled with the random-packing limit of 0.64, so that the maximum concentration is now at $c = 1$. Initially, the particle concentration inside the droplet is uniform at $c = 10^{-3}$, as prescribed by Eq. (27). Because the substrate is smooth, the contact line of the droplet moves continuously toward the droplet center while maintaining a similar shape (i.e., same contact angle) (Fig. 4a).

As the contact line travels inward, more particles accumulate at the contact line, giving rise to a particle concentration peak there (Fig. 4b). Increasing particle concentration at the contact line eventually solidifies this region, and the simulation stops when the particle concentration is close to the random-packing limit.

4.2 Particle concentration and particle area density

The contact line of the droplet described in Fig. 4 stops moving when the particle concentration there approaches the random-packing limit, and the simulation also is halted at this point due to diverging viscosity and diffusivity. Most previous studies have often assumed that the droplet is "dried" at this point, and the particle concentration profile reflects the eventual particle deposition pattern near the contact line [30, 32, 33, 35]. In this section, we offer an argument for why the particle area density, defined as ch, may better reflect the final deposition pattern than the particle concentration does.

The assumption that the final profile of the particle concentration c predicts the actual dried particle deposition pattern may be misleading because particle concentration is the ratio between the number of particles and the available solvent volume. Hence, a high local concentration of particles can be obtained even with a low local number of particles if the available solvent volume is small enough. When this is the case, the particle area density ch is expected to provide a better prediction for the final particle deposition pattern. It was the particle area density that was measured by Deegan and coworkers in their experiments studying the coffee-ring effect (see Fig. 11 of Ref. [42]), and since then this measure has been taken by several researchers as an indication of the actual particle deposition pattern [34, 46, 61, 65, 69, 86].

Figure 5 demonstrates the difference between the final particle concentration and the final particle area density resulting from the simulation shown in Fig. 4. Whereas the particle concentration is highest near the contact line, the particle area density is highest at the droplet center. This difference is due to the fact that most particles remain near the center of the droplet due to a higher volume of suspension there. By examining only the particle-concentration profile, one may conclude that the final particle deposition pattern is similar to a coffee-ring. The particle-area-density profile, however, reflects a final deposition pattern that is more similar to a cone-like deposit at the center of the droplet. Our prediction of
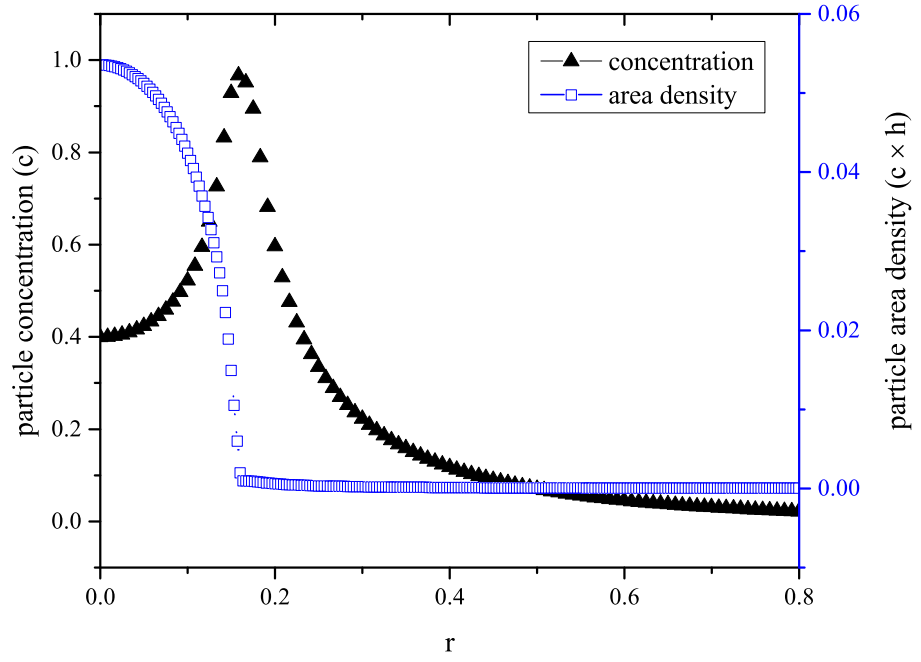
Figure 5: Final profiles for particle concentration (triangle) and area density (square). Values of parameters are: $\theta_e = 9.42^o$ ($A_1 = 3 \times 10^3$ and $A_2 = 10^{-3}$), $I = 10^{-4}$, $b = 10^{-3}$, $Pe = 10^{-4}$, $c_0 = 10^{-3}$.

a cone-like deposit is also consistent with experimental results reported for evaporation of particle-laden droplets on smooth substrates [49, 50, 87].

4.3 Parametric study: Varying evaporation and imbibition rates
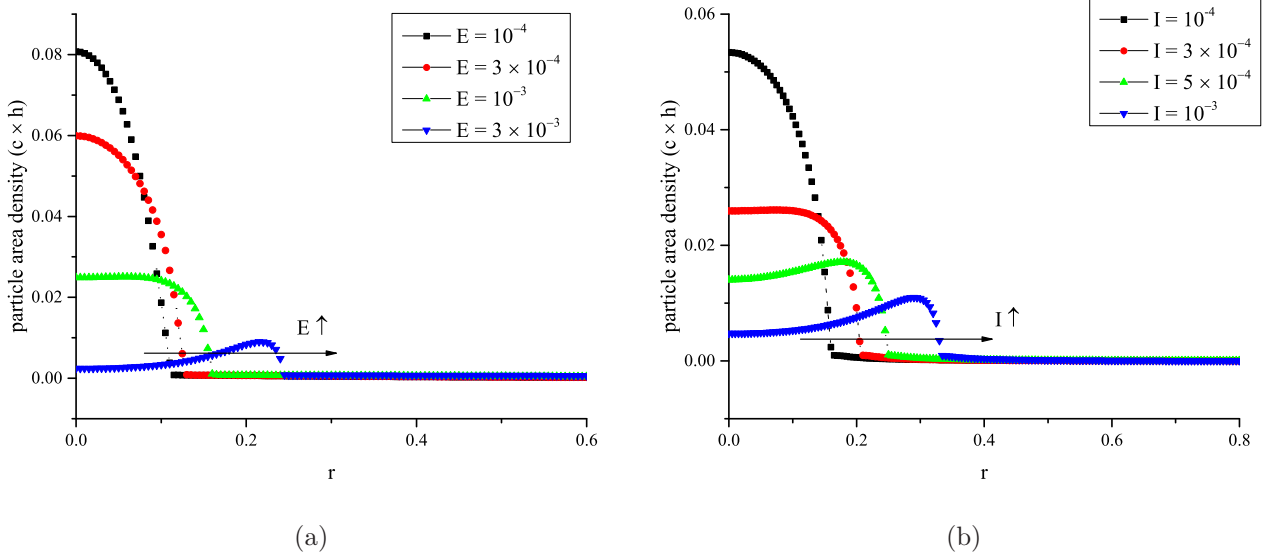

(a)

(b)

Figure 6: Final particle area densities when (a) evaporation rate is increased while imbibition is suppressed, and (b) when imbibition rate is increased while evaporation is suppressed. Values of parameters are: $\theta_e = 9.42^o$ ($A_1 = 3 \times 10^3$ and $A_2 = 10^{-3}$); for (a): $b = 8.18 \times 10^{-4}$, $K = 2 \times 10^{-1}$, $\delta = 10^{-3}$, $Pe = 10^{-4}$, $c_0 = 10^{-3}$; for (b): $b = 10^{-3}$.

Figures 6a and 6b show the final particle-area-density profiles for evaporated and imbibed droplets, respectively. In Fig. 6a, we look at a droplet evaporated on an impermeable smooth substrate, and increase the dimensionless evaporation rate E from 10^{-4} to 3×10^{-3}. Similarly, in Fig. 6b, we increase the dimensionless imbibition rate I while turning off evaporation.

It can be seen from Fig. 6 that at low evaporation and imbibition rates of $E = I = 10^{-4}$, particles are swept by the contact line as it recedes, and the resulting particle deposition pattern is similar to a cone centered at $r = 0$. As the evaporation and imbibition rates are increased, more particles accumulate at the contact line, and the final cone-shaped patterns gradually become more ring-like at high evaporation and imbibition rates. Because the

26

contact-line region solidifies more rapidly with higher solvent loss, final particle deposition patterns at high evaporation and imbibition rates also have wider footprints.

The transition from a cone-like deposit at low solvent-removal rates to a ring-like deposit at high solvent-removal rates can be understood as a competition between diffusive transport and convective transport. In these simulations, we use a Péclet number of $Pe = 10^{-4}$, so setting $E = I = 10^{-4}$ means that the time scale for contact-line retraction due to either evaporation or imbibition is as fast as the time scale for particles to diffuse away from the contact line. As a result, particles are swept toward the droplet center as the contact line recedes. At higher evaporation and imbibition rates, however, particles do not have time to diffuse away and get jammed at the contact line, resulting in wider ring-like patterns.

At intermediate evaporation and imbibition rates of $E = I = 5 \times 10^{-4}$, particle diffusion is still strong enough so that more uniform particle deposition patterns are created. We have also scanned through the parameter space of E and I to look at simultaneous evaporation and imbibition on a smooth substrate. For brevity, those results are not shown here, but they also reveal a similar trend as those in Fig. 6: a cone-to-ring transition occurs as either evaporation or imbibition increases. We can visualize this trend with the phase diagram in Fig. 7.

Two conclusions can be drawn from this section. First, contrary to the usual assertion that substrate-roughness-induced contact-line pinning is the culprit behind the coffee-ring effect [1,42], the results in this section indicate that rings can form even on smooth substrates. The criterion for coffee-ring formation on smooth substrates is that the time scale for contact-line recession has to be much smaller than the time scale for particle diffusion. When the time scale for contact-line motion is greater than particle diffusion time, a cone-shape deposition pattern is obtained.

Second, the results from Fig. 6 also indicate that on smooth substrates, solvent imbibition influences transport of particles the same way as solvent evaporation does. Increasing either
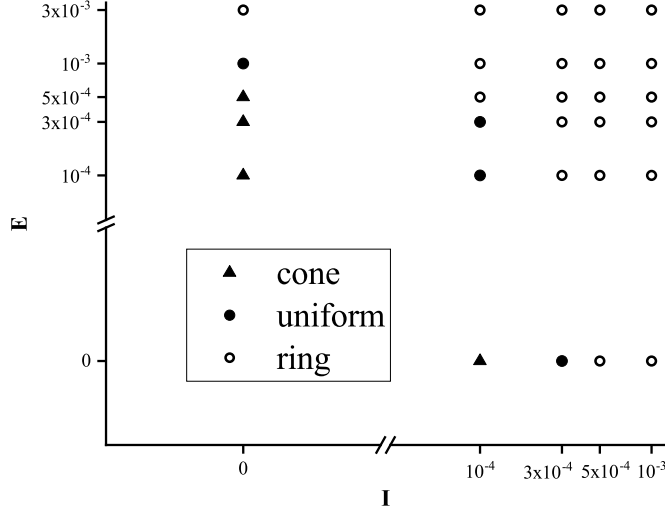
Figure 7: Phase diagram of final particle deposition pattern

solvent-removal rate will induce a cone-to-ring transition for the final particle deposition pattern.

Figures 6 and 7 show model predictions for the case where no contact-line pinning is present. In experiments, contact-line pinning can occur due to substrate roughness, or to particles deposited near the contact line that create an effective substrate roughness. A systematic comparison between the model predictions in Figs. 6 and 7 and experimental observations requires experiments in which contact-line pinning is absent. In a recent work [50], contact-line pinning was prevented by applying a thin coating of silicone oil to a substrate and observing droplet spreading on the oil layer. Consistent with the model predictions, coffee-ring formation is suppressed and colloidal particles get swept to the droplet center. However, a direct comparison with the results presented here cannot be made because there was no substrate imbibition in these experiments and the evaporation rate was not systematically varied.

Finally, we briefly comment on the role of initial particle concentration. We found that for systems with values of imbibition and evaporation rates in the "ring" region of Fig. 7,

increasing the initial particle concentration leads to more cone-like deposits. At high particle concentrations, convective transport of particles to the contact line slows down significantly, and the contact line also becomes solidified faster. As a result, when the maximum particle volume fraction is reached at the contact line, most particles are still near the droplet center. The resulting particle deposition pattern is a cone with a wider footprint.

At low initial particle concentrations, the ring-like deposit structure also becomes more cone-like. This is because the contact line now becomes solidified much later, and as a result, most particles are transported to the droplet center as the contact line sweeps inward. This results in cone-like deposit with a smaller footprint.

5   Particle-laden droplets on rough substrates

In this section, we investigate a particle-laden droplet evaporated and imbibed on a rough substrate. As discussed in Section 3.2, we use a Gaussian bump for the substrate topography η to effectively account for the influence of substrate roughness on contact-line motion. Since the general behavior of imbibed and evaporated droplets is quite similar, we will first discuss how particles are transported when a droplet is imbibed on a rough substrate in Section 5.1.

5.1   Transport of colloidal particles

Figure 8 shows the early time-evolution of the droplet shape and particle concentration as a droplet is imbibed on a rough substrate without evaporation. As mentioned in Section 3.2, a balance between capillary-pressure gradients and disjoining-pressure gradients pins the droplet contact line at the defect. During early stages, solvent evaporation decreases the droplet volume and lowers its apparent contact angle, as seen in Fig. 8a. Figure 8b also shows that a particle concentration peak also quickly forms near the defect due to faster thinning of the droplet near the defect. In many experimental systems, it has been observed
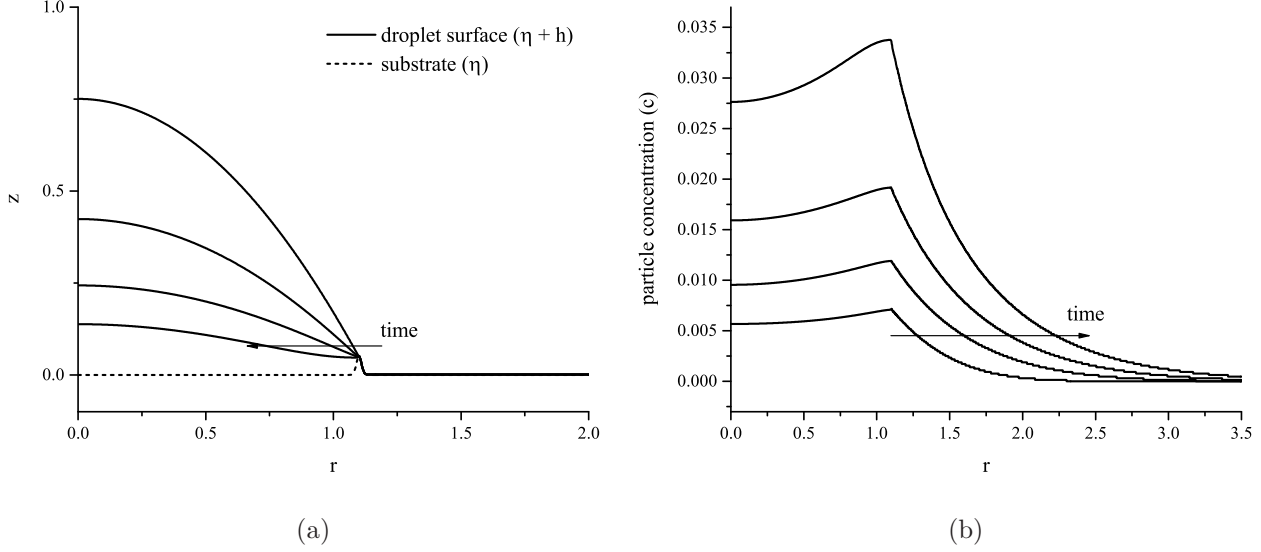
29

Figure 8: Early time-evolution of a droplet laden with particles imbibed on a rough substrate with a Gaussian defect centered at $r = 1.1$ (a) Time-evolution of droplet height h; (b) Time-evolution of particle concentration c. Values of parameters are: $\theta_e = 9.42^o$ ($A_1 = 3 \times 10^3$ and $A_2 = 10^{-3}$), $I = 10^{-4}$, $b = 10^{-3}$, $c_0 = 3 \times 10^{-3}$. The profiles are recorded at $t_1 = 469$, $t_2 = 1409$, $t_3 = 2349$, and $t_4 = 3289$.

that the particles deposited on the substrate near the contact line during this pinned stage can also act as topographical defects and lengthen the pinned stage [17, 49, 71, 88]. This positive-feedback process will ultimately lead to the formation of a dense coffee-ring near the initial contact line with very few particles left near the droplet center.

Figure 9 shows the evolution of the droplet as it undergoes depinning. Depinning occurs when imbibition-induced thinning of droplet causes the liquid-vapor interface near the defect to become unstable. Curve 1 in Fig. 9a shows the interface right before depinning occurs. The balance between capillary-pressure-gradients and disjoining-pressure-gradients at the defect cannot be supported anymore, and the droplet splits into two parts, described by curve 2. There are now a primary droplet centered at $r = 0$ and a "rim" of suspension near the defect. As imbibition of the droplet continues, the contact line of the primary droplet keeps moving toward the droplet center while the contact lines of the rim portion move toward each other, as evident from the transition between curves 2 and 3 of Fig. 9a.
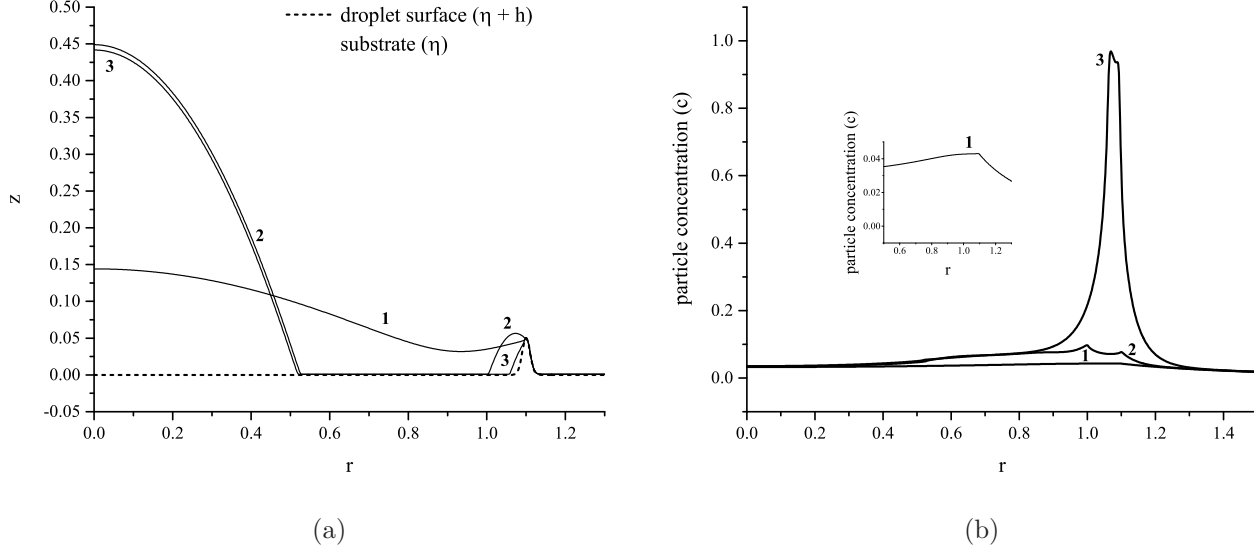
Figure 9: Late time-evolution of a droplet carrying particles being imbibed on a rough substrate with a Gaussian defect centered at $r = 1.1$. (a) Time-evolution of droplet height h; (b) Time-evolution for particle concentration c. Values of parameters are: $\theta_e = 9.42^o$ ($A_1 = 3 \times 10^3$ and $A_2 = 10^{-3}$), $I = 10^{-4}$, $b = 10^{-3}$, $Pe = 10^{-4}$, $c_0 = 3 \times 10^{-3}$. The profiles are recorded at $t_1 = 3486$, $t_2 = 3505$, and $t_3 = 3523$ (labeled 1 through 3, respectively).

Figure 9b shows the late time-evolution of particle concentration inside the droplet. The inset shows a concentration peak near the defect at t_1. As the droplet undergoes depinning at t_2, two new concentration peaks form near the defect, corresponding to the new contact lines of the rim section shown in curve 2 of Fig. 9a. As these two new contact lines move toward each other, the two concentration peaks merge and the random-packing limit is reached, as shown in curve 3 of Fig. 9b. Although droplets with high evaporation and imbibition rates tend to depin faster, we found that increasing either evaporation or imbibition does not qualitatively change the time-evolution of the particle concentration and droplet shape.

5.2   The influence of solvent imbibition

Figure 10 displays the final particle area density profiles for two cases: when only solvent evaporation is present (solid line), and when only solvent imbibition is present (dashed line).
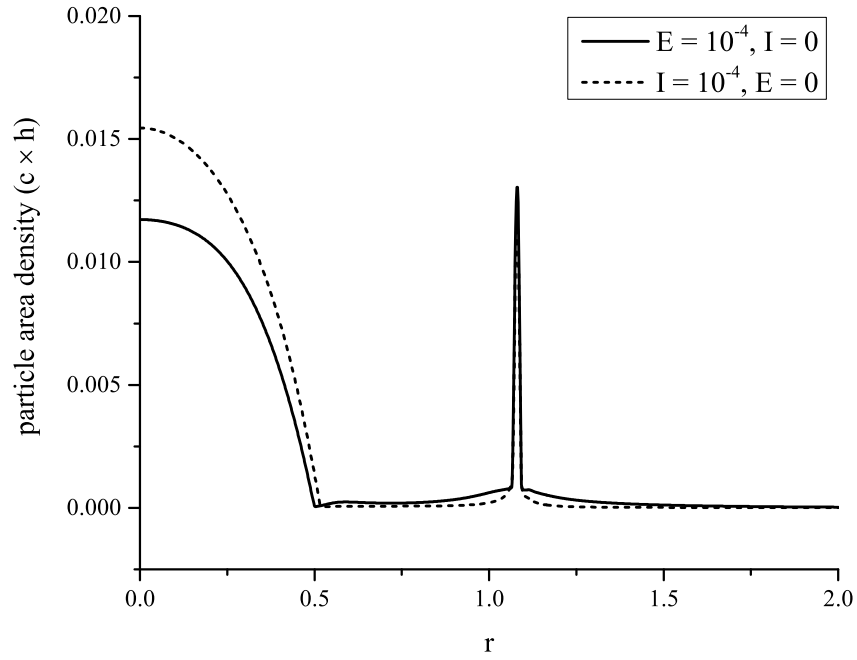
Figure 10: Depinning of contact line results in non-uniform "bullseye" patterns. Values of parameters are: $\theta_e = 9.42^o$ ($A_1 = 3 \times 10^3$ and $A_2 = 10^{-3}$), $Pe = 10^{-4}$, $c_0 = 3 \times 10^{-3}$. For the case with only evaporation (solid lines), $b = 8.18 \times 10^{-4}$, $K = 2 \times 10^{-1}$, $\delta = 10^{-3}$. For the case with only imbibition (dashed lines), $b = 10^{-3}$.

For the case with only solvent imbibition, the parameters are the same as those used in Section 5.1. Both profiles exhibit a "bullseye" deposition pattern: a cone-like region starting from the droplet center followed by a particle-deficient gap (i.e., a depletion zone) surrounded by a dense ring of particles. This bullseye pattern is caused by a rapid contact-line retraction as the droplet depins from the defect. As the contact line retracts to a new location, it drags the particles along with it, leaving behind a depletion zone with very few particles. This prediction is consistent with experimental studies by Morales *et al.* and Zhang *et al.* [49,89], where evaporating droplets undergoing depinning were observed to leave behind a depletion region with few particles. It is also evident from Fig. 10 that on rough substrates, solvent imbibition has the same effect on the final particle deposition pattern as solvent evaporation. In both cases, the droplet contact line drags particles with it after depinning from the defect, resulting in a discontinuous bullseye pattern.

Finally, we briefly discuss the effect of the initial particle concentration. At low initial particle concentrations, we find that the contact line keeps receding after depinning from the defect because the particle concentration at the contact line is not high enough to slow it down. As a result, most particles are transported with the contact line to the droplet center, and the final deposition pattern is cone-like. At high initial particle concentrations, the contact line becomes solidified before depinning, and the final deposition pattern is also a cone, albeit with a wider footprint.

A key motivation of the present paper is to examine whether solvent imbibition and solvent evaporation differ in their effect on the final particle deposition pattern, as suggested by several experimental studies [11,12,15]. The results from Figs. 6 and 10, however, suggest that solvent imbibition and solvent evaporation affect the final particle deposition pattern the same way. Particles that are not irreversibly adsorbed by the substrate move with the contact line as it recedes. Because droplets under solvent imbibition and solvent evaporation exhibit the same contact-line motion, one should expect evaporation and imbibition to have a similar effect on the final particle deposition pattern in the absence of particle adsorption.

Section 6 will explore the important role of particle adsorption on the substrate.

6 Particle adsorption

The results presented in Sections 4 and 5 have shown that evaporation and imbibition are qualitatively similar in their effect on the final particle deposition pattern, a result much different from what has been suggested by previous experimental studies [11, 12, 15]. This is due to the fact that in the absence of particle adsorption onto the substrate, transport of colloidal particles is highly dependent on contact-line motion, which is qualitatively the same for droplet imbibition and droplet evaporation.

The presence of particle adsorption on substrate can significantly affect the final deposition pattern. For example, in their experimental study, Boulogne *et al.* observed that as a droplet containing polystyrene particles is imbibed by a hydrogel, particles inside the droplet are "irreversibly adsorbed on the gel surface", and the particles are not dragged inward with the receding contact line [11]. In this section, we explore whether accounting for particle adsorption can help us explain the experimental results in Refs. [11, 12, 15].

To incorporate particle adsorption into our model, we need to modify the no-penetration boundary condition in Eq. (17) to account for the particle adsorption flux at the substrate $z = \eta(r)$,

$$Dc_z|_{z=\eta(r)} = \alpha c|_{z=\eta(r)}, \tag{28}$$

where α is the adsorption constant, which depends on the interaction potential between the particles and the substrate. Our adsorption model assumes a simple linear relationship between particle concentration near the substrate and adsorption flux, similar to the well-known Langmuir adsorption model, except that for simplicity we do not consider a desorption flux [82]. For simulations involving particle adsorption, we will vary α from 10^{-4} to 10^{-3}, which is within the range calculated using a DLVO potential for various particle-substrate

systems in Ref. [90]. With this modified boundary condition, we have a new evolution equation for particles suspended in the droplet,

$$c_t + \bar{u}c_r = \frac{1}{hrPe}(Dhrc_r)_r + \frac{c}{h}(Ej_e + Ij_i - \alpha). \tag{29}$$

To keep track of the particles adsorbed on the substrate, we also introduce $\Gamma(r,t)$, the adsorbed particle area density, which is related to the average bulk particle concentration by

$$\Gamma_t = \alpha c. \tag{30}$$

For this modified model, we also assume that the particles are smaller than the substrate pore size so that adsorbed particles do not block the substrate pores and reduce solvent imbibition.

6.1 Smooth substrates

First we will study the role of particle adsorption in a droplet of a colloidal suspension imbibed by a smooth substrate. We set our adsorption constant α to 10^{-3} and our imbibition number I to 10^{-4}. Figure 11 shows the time-evolution of the *bulk* area density ch (Fig. 11a) and the *adsorbed* particle area density Γ (Fig. 11b).

Because the adsorption rate α is ten times greater than the imbibition rate I, it can be seen from Fig. 11a that all particles are adsorbed from the bulk onto the substrate at the end of the simulation. As a result, the final adsorbed particle area density closely resembles the starting bulk particle area density (Fig. 11b). This indicates that particle adsorption happens so fast that contact-line retraction has a minimal effect on the final particle area density.

Different final total particle area densities ($\Gamma + c$) for different particle adsorption rates are compared in Fig. 12. It appears that as α decreases, more particles are transported to
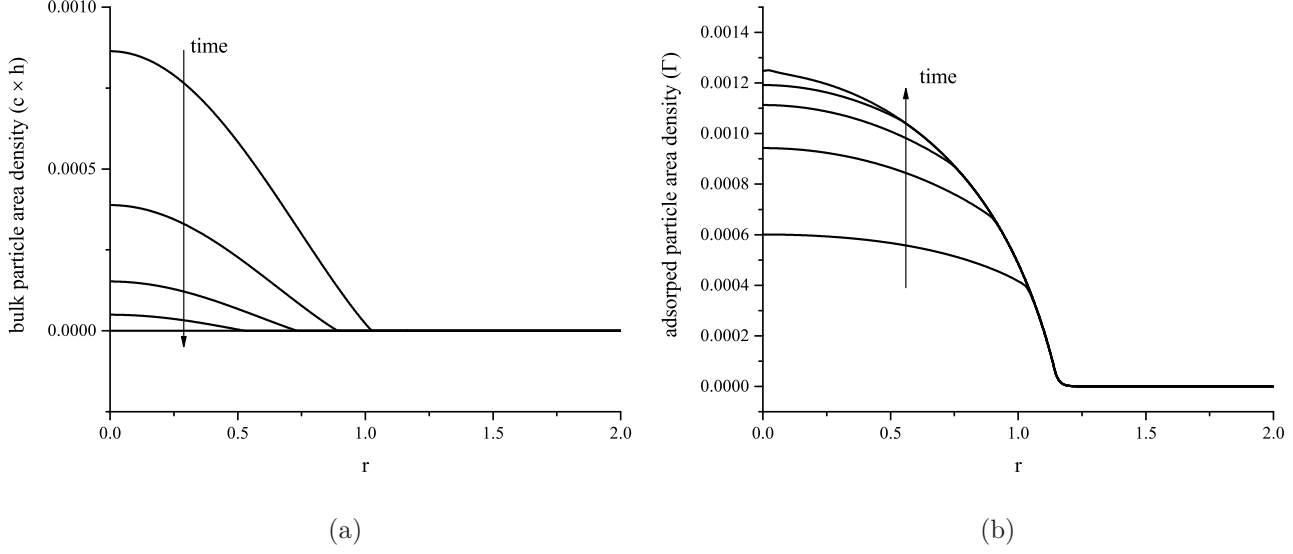
Figure 11: Time-evolution of (a) bulk particle area density and (b) adsorbed particle area density for a droplet imbibed by a smooth substrate. Values of parameters are: $\theta_e = 9.42^o$ ($A_1 = 3 \times 10^3$ and $A_2 = 10^{-3}$), $I = 10^{-4}$, $b = 10^{-3}$, $Pe = 10^{-4}$, $c_0 = 10^{-3}$, $\alpha = 10^{-3}$. The profiles are recorded at $t_1 = 469$, $t_2 = 939$, $t_3 = 1409$, $t_4 = 1879$, and $t_5 = 2379$.

the droplet center, and the final particle deposition pattern becomes more cone-like. This is because when the adsorption rate decreases, more particles remain in the droplet bulk, and are subsequently carried by the contact line toward the droplet center as solvent imbibition proceeds. Conversely, when the adsorption time scale is small compared to the time scale for contact-line motion, more particles are adsorbed in the early stage of contact-line retraction, and the final particle area density becomes more uniform.

6.2   Rough substrates

Figure 13 compares the final particle area densities for different particle adsorption rates for a droplet imbibed by a rough substrate. As in Sections 3.2 and 5, we also use a single Gaussian defect here to represent substrate roughness. Similar to the case with smooth substrates, a fast adsorption rate ($\alpha = 10^{-3}$) causes most particles to be adsorbed on the substrate when the contact line is still pinned to the defect, resulting in a uniform particle
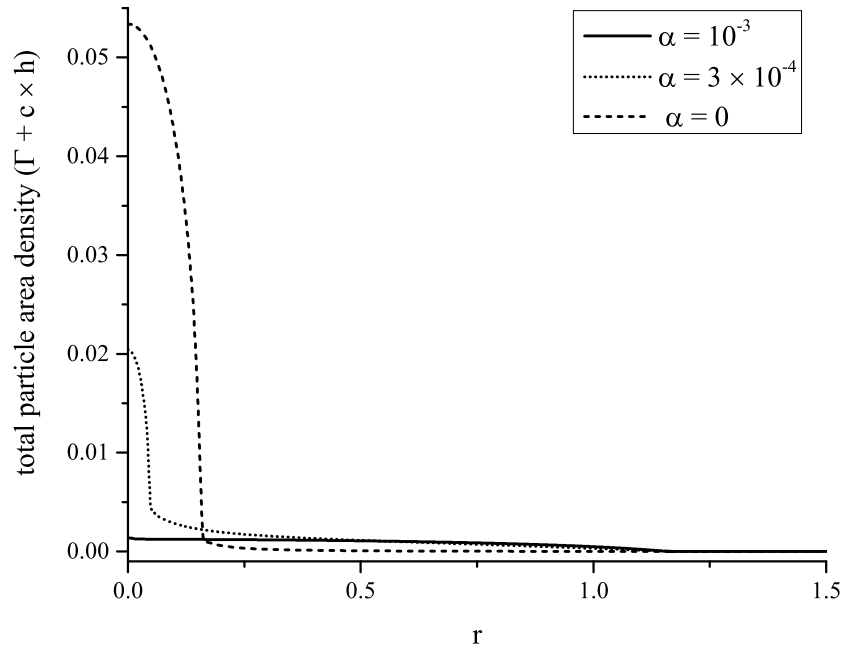
36

Figure 12: Particle area densities resulting from imbibition of a droplet of a colloidal suspension on a smooth substrate. Final particle area density becomes more uniform as particle adsorption increases. Values of parameters are: $\theta_e = 9.42^o$ ($A_1 = 3 \times 10^3$ and $A_2 = 10^{-3}$), $I = 10^{-4}$, $b = 10^{-3}$, $Pe = 10^{-4}$, $c_0 = 10^{-3}$.

deposition pattern. As the adsorption rate decreases, more particles stay in the droplet bulk, and get transported by the contact line as it depins from the defect.
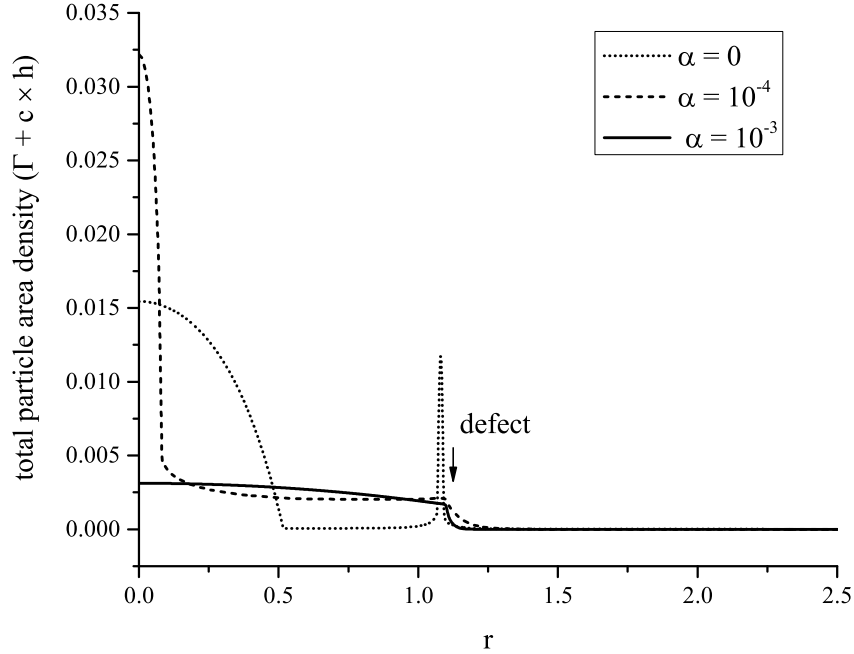

Figure 13: Particle area densities resulting from evaporating a droplet of a colloidal suspension on a rough substrate with a defect centered at $r = 1.1$. Final particle area density becomes more uniform as particle adsorption increases. Values of parameters are: $\theta_e = 9.42^o$ ($A_1 = 3 \times 10^3$ and $A_2 = 10^{-3}$), $I = 10^{-4}$, $b = 10^{-3}$, $Pe = 10^{-4}$, $c_0 = 3 \times 10^{-3}$.

The results from Figs. 12 and 13 suggest that the final particle deposition pattern becomes more uniform as the adsorption rate α increases. This prediction is consistent with the observation made in Ref. [11]. Boulogne *et al.* [11] observed that before the receding stage, most particles are already adsorbed onto the substrate, and do not get dragged inward with the receding contact line.

Similar results were obtained when we ran simulations with only solvent evaporation: when particle adsorption rate is increased, the final particle deposition pattern becomes more uniform on both smooth and rough substrates. These results are similar to experimental results by Bhardwaj *et al.* [90] and more recent simulation results in [86, 91], but for brevity

we do not show them here.

The results of Sections 4 and 5 show that solvent evaporation and solvent imbibition have the same effect on transport of colloidal particles, whereas the results from Refs. [11, 12, 15] suggest that droplet imbibition tends to produce more uniform particle deposition patterns. We believe that the results obtained in this section may help explain the discrepancy. In the case with only evaporation and no imbibition, the right-hand side of Eq. (11) is zero. The presence of solvent imbibition on average will make the velocity field inside the droplet more oriented toward the substrate. As a result, imbibition can bring more particles to the substrate and increase the particle adsorption flux there. Therefore, even though droplet imbibition does not directly lead to more uniform particle deposition patterns, imbibition induces more particle adsorption, and subsequently promotes more uniform deposits.

7 Conclusions

The mathematical model presented in this work provides a starting point to analyze transport of solutes inside droplets undergoing simultaneous imbibition and evaporation, an industrially relevant problem that has not received much attention in prior work. By incorporating disjoining pressure and substrate topography to effectively describe the characteristic stages of contact-line motion as a droplet is evaporated and imbibed, we use our model to examine colloidal particle transport inside droplets during all stages of contact-line motion.

The results reveal that even though the uniform imbibition flux profile is characteristically different from the evaporation flux profile that peaks near the droplet contact line, both evaporation and imbibition are similar in their role of concentrating more particles near the the droplet contact line as it recedes on the substrate. In particular, we have found that on smooth substrates, increasing both evaporation and imbibition will make the final particle deposition pattern undergo a cone-to-ring transition (Section 4). The effect of substrate

roughness was also considered in Section 5, and it was shown that contact-line depinning causes the final particle deposition to become a discontinuous bullseye pattern, a result consistent with previous experimental observations [49, 89]. Because previous theoretical models either assume the contact line is pinned or the contact angle is constant [1, 30, 32–35, 47], they cannot capture this bullseye pattern, which is produced during the transition between the constant-radius stage and the constant-contact-angle stage.

Whereas some recent experimental studies suggest that strong solvent imbibition on permeable substrates results in more uniform final solute deposition patterns, our results in Sections 4 and 5 suggest that both solvent imbibition and solvent evaporation have similar effects on the final particle deposition pattern. This discrepancy suggests that solvent imbibition may not be the direct cause for coffee-ring suppression, but other mechanisms may be at play. We show that one such mechanism, namely particle adsorption on the substrate, can make the final particle deposition pattern more uniform.

This explanation can be supported with droplet imbibition experiments in which particle-substrate attraction is prevented by adjusting the electronic or van der Waals properties of the particles and the substrate. It will also be important to measure the permeability of the substrate [25, 45] and to control contact-line pinning [50]. Because the evaporation flux and imbibition flux act in opposite directions, to fully reveal the role of each process in transport of particles it will be necessary to extend our model to consider a full two-dimensional particle concentration field. This extension is feasible, and has already been done using a lubrication-theory-based framework in the case with only solvent evaporation [32].

8 Acknowledgments

Appendix: Defining contact-line position and contact angles

(a)   (b)
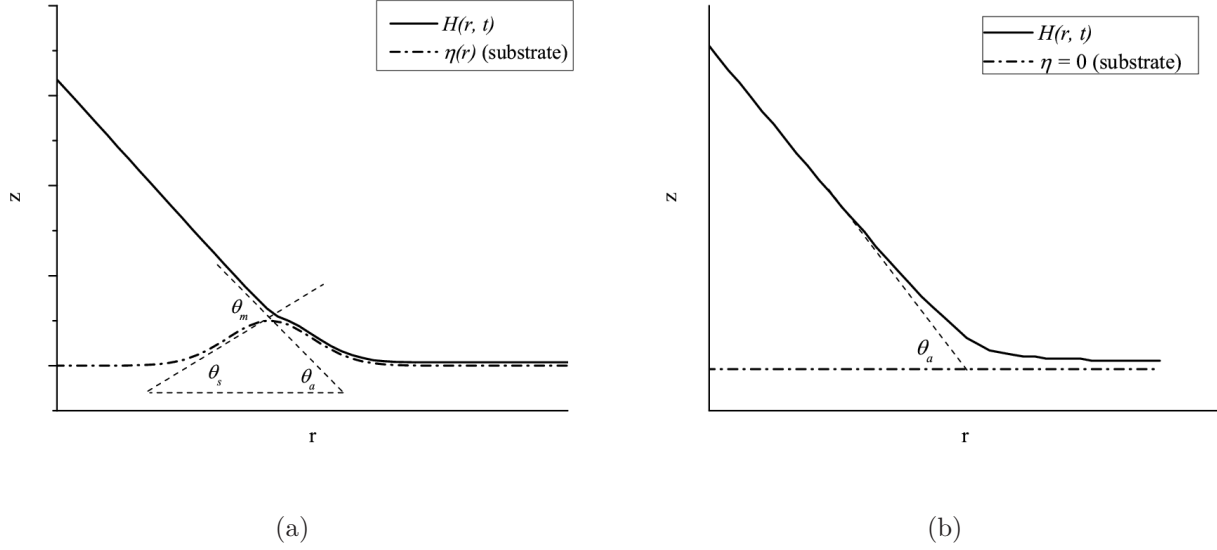
Figure 14: (a) Contact-line region of a droplet near a topographical defect on a substrate. (b) Contact-line region of a droplet on a perfectly smooth substrate.

In this appendix, we discuss how we define contact line and contact angle for our model droplet. To proceed, we need to clarify the distinction between two different kinds of contact angles that arise from our model: the apparent contact angle θ_a and the mesoscopic contact angle θ_m.

For a droplet on a general rough substrate, the mesoscopic contact angle, θ_m, is defined as the greatest angle between the tangent to the liquid-vapor interface and tangent to the substrate [45, 92]. Figure 14a illustrates this definition, and the contact line is then defined as the radial position at which θ_m is found.

When the substrate topography is described by a function $\eta(r)$, the mesoscopic contact angle is given by [45]

$$\tan(\theta_m) = \frac{h_r}{1 + (h_r + \eta_r)\eta_r}. \tag{31}$$

After the contact-line position is located, the apparent contact angle θ_a is defined as the angle between the tangent to the droplet surface and the horizontal plane evaluated at the

contact-line position (Fig. 14a). The difference between θ_m and θ_a is

$$\theta_m - \theta_a = \theta_s, \tag{32}$$

where θ_s is the angle the tangent to the topography $\eta(r)$ forms with the horizontal plane (Fig. 14a). It can be seen from Eq. (32) that on a perfectly smooth substrate, the apparent contact angle is the same as the mesoscopic contact angle (Fig. 14b).

References

[1] R. D. Deegan, O. Bakajin, T. F. Dupont, G. Huber, S. R. Nagel, and T. A. Witten. Capillary Flow as the Cause of Ring Stains from Dried Liquid Drops. *Nature*, 389(6653):827–829, 1997.

[2] J. Park and J. Moon. Control of Colloidal Particle Deposit Patterns within Picoliter Droplets Ejected by Ink-jet Printing. *Langmuir*, 22(8):3506–3513, 2006.

[3] C. Girotto, B. P. Rand, J. Genoe, and P. Heremans. Exploring Spray Coating as a Deposition Technique for the Fabrication of Solution-Processed Solar Cells. *Sol. Energy Mater. Sol. Cells*, 93(4):454–458, 2009.

[4] M. Majumder, C. Rendall, M. Li, M. Behabtu, J. A. Eujel, R. H. Hauge, H. K. Schmidt, and M. Pasquali. Insights into the Physics of Spray Coating of SWNT Films. *Chem. Eng. Sci.*, 65(6):2000–2008, 2010.

[5] Y. L. Kong, I. Tamargo, H. Kim, B. N. Johnson, M. K. Gupta, T. Koh, H. Chin, D. Steingart, B. P. Rand, and M. C. McAlpine. 3D Printed Quantum Dot Light-Emitting Diodes. *Nano Lett.*, 14(12):7017–7023, 2014.

[6] B. J. de Gans and U. S. Schubert. Inkjet Printing of Well-Defined Polymer Dots and Arrays. *Langmuir*, 20(18):7789–7793, 2004.

[7] J. Z. Wang, Z. H. Zheng, H. W. Li, W. T. S. Huck, and H. Sirringhaus. Dewetting of Conducting Polymer Inkjet Droplets on Patterned Surfaces. *Nat. Mater.*, 3(3):171–176, 2004.

[8] S. Maheshwari, L. Zhang, Y. Zhu, and H.-C. Chang. Coupling between Precipitation and Contact-Line Dynamics: Multiring Stains and Stick-Slip Motion. *Phys. Rev. Lett.*, 100:044503, 2008.

[9] J. R. Trantum, D. W. Wright, and F. R. Haselton. Biomarker-Mediated Disruption of Coffee-Ring Formation as a Low Resource Diagnostic Indicator. *Langmuir*, 28(4):2187–2193, 2012.

[10] J. T. Wen, C. M. Ho, and P. B. Lillehoj. Coffee-Ring Aptasensor for Rapid Protein Detection. *Langmuir*, 29(26):8440–8446, 2013.

[11] F. Boulogne, F. Ingremeau, J. Dervaux, L. Limat, and H. A. Stone. Homogeneous deposition of particles by absorption on hydrogels. *Euro. Phys. Lett.*, 112:48004, 2015.

[12] A. Nilghaz, L. Zhang, and W. Shen. Coffee stains on paper. *Chem. Eng. Sci.*, 129:34–41, 2015.

[13] A. Nilghaz, L. Guan, W. Tan, and W. Shen. Advances of Paper-Based Microfluidics for Diagnostics - The Original Motivation and Current Status. *ACS Sens.*, 1(12):1382–1393, 2016.

[14] A. Määttänen, D. Fors, S Wang, D. Valtakari, P. Ihalainen, and J. Peltonen. Paper-based planar reaction arrays for printed diagnostics. *Sens. Actuators B*, 160:1404–1412, 2011.

[15] M. Pack, H. Hu, D.-O. Kim, X. Yang, and Y. Sun. Colloidal Drop Deposition on Porous Substrates: Competition among Particle Motion, Evaporation, and Infiltration. *Langmuir*, 8(29):4704–4709, 2015.

[16] R. Dou and B. Derby. Formation of Coffee Stains on Porous Surfaces. *Langmuir*, 28(12):5331–5338, 2012.

[17] D. Orejon, K. Sefiane, and M. E. R. Shanahan. Stick-Slip of Evaporating Droplets: Substrate Hydrophobicity and Nanoparticle Concentration. *Langmuir*, 27(21):12834–12843, 2011.

[18] V. M. Starov, S. R. Kostvintsev, V. D. Sobolev, M. G. Velarde, and S. A. Zhdanov. Spreading of liquid drops over saturated porous layers. *J. Colloid Interface Sci.*, 246:372–379, 2002.

[19] S. M. Kumar and A. P. Deshpande. Dynamics of drop spreading on fibrous porous media. *Colloids Surf. A*, 277:157–163, 2006.

[20] T. A. H. Nguyen, A. V. Nguyen, M. A. Hampton, Z. P. Xu, L. Huang, and V. Rudolph. Theoretical and Experimental Analysis of Droplet Evaporation on Solid Surfaces. *Chem. Eng. Sci.*, 69(1):522–529, 2012.

[21] D. Debuisson, V. Senez, and S. Arscott. Tunable Contact Angle Hysteresis by Micropatterning Surfaces. *Appl. Phys. Lett.*, 98:184101, 2011.

[22] D. Debuisson, A. Merlen, V. Senez, and S. Arscott. Stick-Jump (SJ) Evaporation of Strongly Pinned Nanoliter Volume Sessile Water Droplets on Quick Drying, Micropatterned Surfaces. *Langmuir*, 32(11):2679–2686, 2016.

[23] J. M. Stauber, S. K. Wilson, B. R. Duffy, and K. Sefiane. On the Lifetimes of Evaporating Droplets. *J. Fluid Mech.*, 744:R2, 2014.

[24] J. M. Stauber, S. K. Wilson, B. R. Duffy, and K. Sefiane. On the Lifetimes of Evaporating droplets with Related Initial and Receding Contact Angles . *Phys. Fluids*, 27:122101, 2015.

[25] Z. Wang, L. Espín, F. S. Bates, S. Kumar, and C. W. Macosko. Water droplet spreading and imbibition on superhydrophilic poly(butylene terephthalate) melt-blown fiber mats. *Chem. Eng. Sci.*, 146:104–114, 2016.

[26] G. Wells, R.-G. Élfego, Y. E. Lirzin, A. Nourry, B. V. Orme, M. Pradas, and R. Ledesma-Aguilar. Snap evaporation of droplets on smooth topographies. *Nat. Commun.*, 9:1380, 2018.

[27] V. S. Ajaev. Spreading of Thin Volatile Liquid Droplets on Uniformly Heated Surfaces. *J. Fluid Mech.*, 528(2):279–296, 2005.

[28] C. Sodtke, V. S. Ajaev, and P. Stephan. Dynamics of Volatile Liquid Droplets on Heated Surfaces: Theory versus Experiment. *J. Fluid Mech.*, 610:343–362, 2008.

[29] N. Murisic and L. Kondic. Modeling Evaporation of Sessile Drops with Moving Contact Lines. *Phys. Rev. E*, 78(6):1–4, 2008.

[30] R. V. Craster, O. K. Matar, and K. Sefiane. Pinning, Retraction and Terracing of Evaporating Droplets Containing Nanoparticles. *Langmuir*, 25(6):3601–3609, 2009.

[31] N. Murisic and L. Kondic. On Evaporation of Sessile Drops with Moving Contact Lines. *J. Fluid Mech.*, 679:219–246, 2011.

[32] K. L. Maki and S. Kumar. Fast Evaporation of Spreading Droplets of Colloidal Suspensions. *Langmuir*, 27(18):11347–11363, 2011.

[33] L. Espín and S. Kumar. Sagging of Evaporating Droplets of Colloidal Suspensions on Inclined Substrates. *Langmuir*, 30(40):11966–11974, 2014.

[34] A. W. Wray, D. T. Papageorgiou, R. V. Craster, K. Sefiane, and O. K. Matar. Electrostatic Suppression of the "Coffee Stain Effect". *Langmuir*, 30(20):5849–5858, 2014.

[35] G. Karapetsas, K. C. Sahu, and O. K. Matar. Evaporation of Sessile Droplets Laden with Particles and Insoluble Surfactants. *Langmuir*, 32:6871–6881, 2016.

[36] A. Amini and G. M. Homsy. Evaporation of Liquid Droplets on Solid Substrates. I. Flat Substrate with Pinned or Moving Contact Line. *Phys. Rev. Fluids*, 2:043603, 2017.

[37] A. Amini and G. M. Homsy. Evaporation of Liquid Droplets on Solid Substrates. II. Periodic Substrates with Moving Contact Lines. *Phys. Rev. Fluids*, 2:043604, 2017.

[38] V. M. Starov, S. R. Kostvintsev, V. D. Sobolev, M. G. Velarde, and S. A. Zhdanov. Spreading of liquid drops over dry porous layers: complete wetting case. *J. Colloid Interface Sci.*, 252:397–408, 2002.

[39] N. Alleborn and H. Raszillier. Spreading and Sorption of a Droplet on a Porous Substrate. *Chem. Eng. Sci.*, 59(10):2071–2088, 2004.

[40] A. Zadražil, F. Stepanek, and O. K. Matar. Droplet Spreading, Imbibition and Solidification on Porous Media. *J. Fluid Mech.*, 562:1–33, 2006.

[41] C. Christodoulou, E. Sorensen, S. García-Muñoz, and L. Mazzei. Mathematical modelling of water absorption and evaporation in a pharmaceutical tablet during film coating. *Chem. Eng. Sci.*, 175:40–55, 2018.

[42] R. D. Deegan, O. Bakajin, T. F. Dupont, G. Huber, S. R. Nagel, and T. A. Witten. Dynamic Self-Assembly of Polymer Colloids To Form Linear Patterns. *Phys. Rev. E*, 62(1):756–765, 2000.

[43] H. Hu and R. G. Larson. Evaporation of a Sessile Droplet on a Substrate. *J. Phys. Chem. B*, 106(6):1334–1344, 2002.

[44] H. Masoud and J. D. Felske. Analytical Solution for Inviscid Flow inside an Evaporating Sessile Drop. *Phys. Rev. E*, 79(1):016301, 2009.

[45] L. Espín and S. Kumar. Droplet Spreading and Absorption on Rough, Permeable Substrates. *J. Fluid Mech.*, 784:465–486, 2015.

[46] T. Pham and S. Kumar. Drying of Droplets of Colloidal Suspensions on Rough Substrates. *Langmuir*, 33(38):10061–10076, 2017.

[47] P. J. Sáenz, A. W. Wray, Z. Che, O. K. Matar, P. Valluri, J. Kim, and K. Sefiane. Dynamics and Universal Scaling Law in Geometrically-Controlled Sessile Drop Evaporation. *Nat. Commun.*, 8:14783, 2017.

[48] L. Espín and S. Kumar. Droplet Wetting Transitions on Inclined Substrates in the Presence of External Shear and Substrate Permeability. *Phys. Rev. Fluids*, 2:014004, 2017.

[49] V. Morales, J.-Y. Pariange, M. Wu, F. J. Pérez-Eche, W. Zhang, W. Sang, and T. S. Steenhuis. Surfactant-Mediated Control of Colloid Pattern Assembly and Attachment Strength in Evaporating Droplets. *Langmuir*, 29(6):1831–1840, 2013.

[50] S. Das, A. Dey, G. Reddy, and D. D. Sarma. Suppression of the Coffee-Ring Effect and Evaporation-Driven Disorder to Order Transition in Colloidal Droplets. *J. Phys. Chem. Lett.*, 8:4704–4709, 2017.

[51] M. N. Popescu, G. Oshanin, S. Dietrich, and A.-M. Cazabat. Precursor Films in Wetting Phenomena. *J. Phys.: Condens. Matter*, 24:243102–243132, 2012.

[52] W. B. Russel, D. A. Saville, and W. R. Schowalter. *Colloidal Dispersions*. Cambridge University Press, 1989.

[53] N. Savva and S. Kalliadasis. Dynamics of Moving Contact Lines: A Comparison Between Slip and Precursor-Film Models. *Europhys. Lett.*, 94:64004, 2011.

[54] D. M. Anderson and S. H. Davis. Spreading of thin volatile liquid droplets on uniformly heated surfaces. *Physics of Fluids*, 7(2):248–265, 1995.

[55] L. M. Hocking. A moving fluid interface on a rough surface. *J. Fluid. Mech.*, 76(4):801–817, 1976.

[56] C.-Y. Liu, E. Vandre, M. S. Carvalho, and S. Kumar. Dynamic wetting failure in surfactant solutions. *J. Fluid. Mech.*, 789:285–309, 2016.

[57] Xuemin Ye, Xiangshan Zhang, Minglan Li, Chunxi Li, and Shuai Dong. Contact line dynamics of two-dimensional evaporating drops on heated surfaces with temperature-dependent wettabilities. *Int. J. Heat Mass Transfer*, 128:1263–1279, 2019.

[58] L. W. Schwartz and R. R. Eley. Simulation of Droplet Motion on Low-Energy and Heterogeneous Surfaces. *J. Colloid Interface Sci.*, 202:173–188, 1998.

[59] L. W. Schwartz. Hysteretic Effects in Droplet Motions on Heterogeneous Substrates: Direct Numerical Simulation. *Langmuir*, 14:3440–3453, 1998.

[60] J. Park and S. Kumar. Droplet Sliding on an Inclined Substrate with a Topographical Defect. *Langmuir*, 33(29):7352–7363, 2017.

[61] L. Fraštia, A. J. Archer, and U. Thiele. Modelling the Formation of Structured Deposits at Receding Contact Lines of Evaporating Solutions and Suspensions. *Soft Matter*, 8(44):11363–11386, 2012.

[62] A. Oron, S. H. Davis, and S. G. Bankoff. Long-Scale Evolution of Thin Liquid Films. *Rev. Mod. Phys.*, 69(3):931–980, 1997.

[63] S. H. Davis and L. M. Hocking. Spreading and imbibition of viscous liquid on a porous base. *Phys. Fluids*, 11:48–57, 1999.

[64] J. P. Burelbach, S. G. Bankoff, and S. H. Davis. Nonlinear Stability of Evaporating/Condensing Liquid Films. *J. Fluid Mech.*, 195:463–494, 1988.

[65] M. R. E. Warner, R. V. Craster, and O. K. Matar. Surface Patterning via Evaporation of Ultrathin Films Containing Nanoparticles. *J. Colloid Interface Sci.*, 267(1):92–110, 2003.

[66] V. S. Ajaev. Viscous Flow of a Volatile Liquid on an Inclined Heated Surface. *J. Colloid Interface Sci.*, 280(1):165–173, 2004.

[67] O. K. Matar, R. V. Craster, and K. Sefiane. Dynamics Spreading of Droplets Containing Nanoparticles. *Phys. Rev. E*, 76(5):056315, 2007.

[68] A.-M. Cazabat and G. Guéna. Evaporation of Macroscopic Sessile Droplets. *Soft Matter*, 6(10):2591–2612, 2010.

[69] T. Pham, X. Cheng, and S. Kumar. Drying of Multicomponent Thin Films on Substrates with Topography. *J. Polym. Sci. Part B: Polym. Phys.*, 55:1681–11691, 2017.

[70] H. Hu and R. G. Larson. Analysis of the Microfluid Flow in an Evaporating Sessile Droplet. *Langmuir*, 21(9):3963–3971, 2005.

[71] R. G. Larson. Transport and Deposition Patterns in Drying Sessile Droplets. *AIChE J.*, 60(5):1538–1571, 2014.

[72] S. Sultan, A. Boudaoud, and M. B. Amar. Evaporation of a Thin Film: Diffusion of the Vapour and Marangoni Instabilities. *J. Fluid Mech.*, 543:183–202, 2005.

[73] A. H. Persad and C. A. Ward. Expressions for the Evaporation and Condensation Coefficients in the Hertz-Knudsen Relation. *Chemical Reviews*, 116:7727–7767, 2016.

[74] R. W. Schrage. *A Theoretical Study of Interphase Mass Transfer*. PhD thesis, Columbia University, 1953.

[75] H. J. Palmer. The Hydrodynamic Stability of Rapidly Evaporating Liquids at Reduced Pressure. *J. Fluid Mech.*, 75(3):487–511, 1976.

[76] V. S. Ajaev, T. Gambaryan-Roisman, and P. Stephan. Static and Dynamic Contact Angles of Evaporating Liquids on Heated Surfaces. *J. Colloid Interface Sci.*, 342(2):550–558, 2010.

[77] O. E. Jensen and J. B. Grotberg. The Spreading of Heat or Soluble Surfactant along a Thin Liquid Film. *Phys. Fluids A*, 5(1):58–68, 1993.

[78] G. K. Batchelor. Brownian Diffusion of Particles with Hydrodynamic Interactions. *J. Fluid Mech.*, 74(1):1–29, 1976.

[79] S. G. Yiantsios and B. G. Higgins. A Mechanism of Marangoni Instability in Evaporating Thin Liquid Films Due to Soluble Surfactant. *Phys. Fluids*, 22(2):022102, 2010.

[80] L. Espín and S. Kumar. Forced Spreading of Films and Droplets of Colloidal Suspensions. *J. Fluid Mech.*, 742:495–519, 2014.

[81] H. H. Kausch, D. G. Fesko, and N. W. Tschoegl. The random packing of circles in a plane. *J. Colloid Interface Sci.*, 37:603–611, 1971.

[82] J. Berg. *Interfaces and Colloids.* World Scientific, 2014.

[83] P. N. Brown, A. C. Hindmarsh, and L. R. Petzold. Using Krylov Methods in the Solution of Large-Scale Differential-Algebraic Systems. *SIAM J. Sci. Comput.*, 15(6):1467–1488, 1994.

[84] L. H. Tanner. The Spreading of Silicone Oil Drops on Horizontal Surfaces. *J. Phys. D: Appl. Phys.*, 12(09):1473–1484, 1979.

[85] J. Eggers and L. M. Pismen. Nonlocal Description of Evaporating Drops. *Phys. Fluids*, 22:112101, 2010.

[86] A. Zigelman and O. Manor. The deposition of colloidal particles from a sessile drop of a volatile suspension subject to particle adsorption and coagulation. *J. Colloid Interface Sci.*, 509:195–208, 2018.

[87] K. A. Baldwin, S. Roest, D. J. Fairhurst, K. Sefiane, and M. E. R. Shanahan. Monolith Formation and Ring-Stain Suppression in Low-Pressure Evaporation of Poly(ethylene oxide) Droplets. *J. Fluid Mech.*, 695:321–329, 2012.

[88] R. D. Deegan. Pattern formation in drying drops. *Phys. Rev. E*, 61(1):475–485, 2000.

[89] W. Zhang, T. Yu, L. Liao, and Z. Cao. Ring formation from a drying sessile colloidal droplet . *AIP Advances*, 3:102109, 2013.

[90] R. Bhardwaj, X. Fang, P. Somasundaran, and D. Attinger. Self-Assembly of Colloidal Particles from Evaporating Droplets: Role of DLVO Interactions and Proposition of a Phase Diagram. *Langmuir*, 26(11):7833–7842, 2010.

[91] D. P. Siregar, J. G. M. Kuerten, and C. W. M. van der Geld. Numerical simulation of the drying of inkjet-printed droplets. *J. Colloid Interface Sci.*, 392:388–395, 2013.

[92] N. Savva and S. Kalliadasis. Two-Dimensional Droplet Spreading over Topographical Substrates. *Phys. Fluids*, 21:092102, 2009.